



UPPSALA  
UNIVERSITET

*Digital Comprehensive Summaries of Uppsala Dissertations  
from the Faculty of Medicine 1907*

# Visualising neurodegeneration in the living brain

*Preclinical evaluation of PET radioligands*

MENGFEI XIONG



ACTA  
UNIVERSITATIS  
UPSALIENSIS  
UPPSALA  
2023

ISSN 1651-6206  
ISBN 978-91-513-1727-4  
URN urn:nbn:se:uu:diva-497274

Dissertation presented at Uppsala University to be publicly examined in Rudbecksalen, Rudbecklaboratoriet, Dag Hammarskjölds Väg 20, Uppsala, Friday, 14 April 2023 at 13:00 for the degree of Doctor of Philosophy (Faculty of Medicine). The examination will be conducted in English. Faculty examiner: Professor Per Borghammer (Department of Clinical Medicine - Nuclear Medicine and PET, Aarhus University, Denmark).

### Abstract

Xiong, M. 2023. Visualising neurodegeneration in the living brain. Preclinical evaluation of PET radioligands. *Digital Comprehensive Summaries of Uppsala Dissertations from the Faculty of Medicine* 1907. 70 pp. Uppsala: Acta Universitatis Upsaliensis. ISBN 978-91-513-1727-4.

With an ageing population, the number of people suffering from Alzheimer's disease (AD) and Parkinson's disease (PD) escalates yearly. Pathological hallmarks of AD and PD include aggregated proteins and synaptic dysfunction. Developing imaging probes targeting specific pathological hallmarks is highly valuable in aiding early diagnosis and treatment assessment.

The thesis focused on evaluating positron emission tomography (PET) imaging probes that can visualise different pathological changes in preclinical models of neurodegeneration. Ligands targeting synaptic vesicle protein 2A (SV2A), alpha-synuclein ( $\alpha$ Syn), and amyloid-beta ( $A\beta$ ) are investigated.

In paper I, we compared synaptic density in transgenic AD and PD mouse models to their wild-type age-matched controls using SV2A PET. In the hippocampus, lower synaptic density was found in the PD mice compared to the control. In paper II, we continued using SV2A PET and studied synaptic density in ageing mice. Synaptic density remained steady for most of the lifespan but slightly decreased in old age. In paper III, we developed and evaluated five antibody-based PET radioligands targeting  $\alpha$ Syn aggregates. By conjugating anti- $\alpha$ Syn antibodies with the transferrin receptor (TfR) binder 8D3, we increased antibody brain entry significantly. These bispecific antibodies displayed high specificity and selectivity to  $\alpha$ Syn aggregates. The most promising candidate successfully imaged brain-deposited  $\alpha$ Syn but was unable to detect endogenously expressed  $\alpha$ Syn in PD mouse models. In light of this, further investigation of antibody brain entry, distribution, and elimination is needed. Thus, in paper IV, we used microdialysis to compare the brain pharmacokinetics of a bispecific antibody targeting TfR and  $A\beta$  and its regular monospecific version that only binds to  $A\beta$ . The bispecific antibody showed distinct pharmacokinetics and entered the brain more efficiently than the regular antibody. Lastly, in paper V, we studied the impact of anti- $A\beta$  antibody treatment on amyloid PET. AD mice were short-term treated with anti- $A\beta$  antibody mAb158 and underwent [ $^{11}$ C]PiB *ex vivo* autoradiography. We found a trend indicating that the treatment reduced the [ $^{11}$ C]PiB signal despite no reduction in total  $A\beta$  levels.

Our results contribute to an increased understanding of PET radioligands imaging neurodegeneration. Furthermore, it provides valuable information for designing and developing new PET radioligands.

**Keywords:** Positron emission tomography (PET), Alzheimer's disease, Parkinson's disease, SV2A, neurodegeneration, immunotherapy, transgenic mice

*Mengfei Xiong, Department of Public Health and Caring Sciences, Geriatrics, Box 609, Uppsala University, SE-75125 Uppsala, Sweden.*

© Mengfei Xiong 2023

ISSN 1651-6206

ISBN 978-91-513-1727-4

URN urn:nbn:se:uu:diva-497274 (<http://urn.kb.se/resolve?urn=urn:nbn:se:uu:diva-497274>)

*“Though the journey is far and long, I shall search up and down.”*  
—*Qu Yuan*



# List of Papers

This thesis is based on the following papers, which are referred to in the text by their Roman numerals.

- I. **Xiong, M.**, Roshanbin, S., Rokka, J., Schlein, E., Ingelsson, M., Sehlin, D., Eriksson, J. and Syvänen, S. (2021) In vivo imaging of synaptic density with [<sup>11</sup>C]UCB-J PET in two mouse models of neurodegenerative disease. *Neuroimage*, 239, 118302.
- II. **Xiong, M.**, Roshanbin, S., Sehlin, D., Hansen, D., Knudsen, G., Rokka, J., Eriksson, J. and Syvänen, S. Synaptic density in aging mice measured by [<sup>18</sup>F]SynVesT-1 PET. *Under review*
- III. Roshanbin, S., **Xiong, M.**, Hultqvist, G., Söderberg, L., Zachrisson, O., Meier, S., Ekmark-Lewén, S., Bergström, J., Ingelsson, M., Sehlin, D. and Syvänen, S. (2022) In vivo imaging of alpha-synuclein with antibody-based PET. *Neuropharmacology*, 208, 108985.
- IV. Julku, U., **Xiong, M.**, Wik, E., Roshanbin, S., Sehlin, D., Syvänen, S. Brain pharmacokinetics of mono- and bispecific amyloid- $\beta$  antibodies in wild-type and Alzheimer's disease mice measured by high cut-off microdialysis. (2022) *Fluids Barriers CNS*, 19, 99.
- V. **Xiong, M.**, Dahlén A., Roshanbin S., Aguilar, X., Eriksson, J., Sehlin, D. and Syvänen, S. [<sup>11</sup>C]PiB binding after treatment with an amyloid-beta antibody. *Manuscript*.

Reprints were made with permission from the respective publishers.

## Additional publications

- I. Shalgunov, V.\*, **Xiong, M.\***, L'Estrade, E.T., Raval, N.R., Andersen, I.V., Edgar, F.G., Speth, N.R., Bærentzen, S.L., Hansen, H.D., Donovan, L.L. and Nasser, A. (2020) Blocking of efflux transporters in rats improves translational validation of brain radioligands. *EJNMMI research*, 10(1), 1-11. (\*: shared first authorship)
- II. Roshanbin, S., Julku, U., **Xiong, M.**, Eriksson, J., Masliah, E., Hultqvist, G., Bergström, J., Ingelsson, M., Syvänen, S. and Sehlin, D. (2022) Reduction of  $\alpha$ SYN Pathology in a Mouse Model of PD Using a Brain-Penetrating Bispecific Antibody. *Pharmaceutics*, 14(7), 1412.
- III. Syvänen, S., Meier, S. R., Roshanbin, S., **Xiong, M.**, Faresjö, R., Gustavsson, T., Bonvicini, G., Schlein, E., Aguilar, X., Julku, U., Eriksson, J., & Sehlin, D. (2022). PET Imaging in Preclinical Anti-A $\beta$  Drug Development. *Pharmaceutical research*, 39(7), 1481–1496.

# Contents

Introduction.....	11
Neurodegenerative diseases .....	11
Parkinson's diseases .....	11
Alpha-synuclein .....	12
Alzheimer's disease.....	14
Amyloid-beta.....	15
Ageing synapse .....	15
PET imaging of AD and PD.....	16
Antibody PET.....	18
Quantification of dynamic PET images .....	21
Methodology.....	23
Animal models .....	23
Establishment of an $\alpha$ Syn deposition model .....	24
Antibodies .....	25
Radiolabelling .....	26
Autoradiography.....	28
PET/CT imaging .....	29
Kinetic analysis of radioligand binding.....	30
Microdialysis.....	32
Brain homogenisation .....	33
Thin-layer chromatography.....	34
Enzyme-linked immunosorbent assay.....	34
Staining .....	35
Funding .....	36
Aim .....	37
Results and discussion .....	38
Synaptic density change in neurodegenerative disease .....	38
Synaptic density in ageing.....	40
Quantification of SV2A PET .....	41
Visualising $\alpha$ Syn with antibody-PET.....	42
Understanding the pharmacokinetics of bispecific antibodies .....	43
Antibody treatment effect on PET imaging .....	44
Conclusion and future perspectives .....	46

Popular science summary .....	48
Acknowledgements.....	51
References.....	54

# Abbreviations

AADC	Aromatic amino-acid decarboxylase
A $\beta$	Amyloid-beta
AD	Alzheimer's disease
APP	Amyloid-beta precursor protein
AUC	Area under the curve
$\alpha$ Syn	Alpha-synuclein
B <sub>max</sub>	Target density
Bq	Becquerel
BW	Body weight
CA	Cornu ammonis
C <sub>img</sub>	Image-derived radioactivity concentration
C <sub>p</sub>	Radioactivity concentration in plasma (blood)
C <sub>T</sub>	Radioactivity concentration in tissue (brain)
CSF	Cerebrospinal fluid
CT	Computed tomography
Da	Dalton
DLB	Dementia with Lewy bodies
EC	Electron capture
FA	Formic acid
FOV	Field of view
GABA	Gamma-Aminobutyric Acid
GFAP	Glial fibrillary acidic protein
HRP	Horseradish peroxidase
Iba	Ionised calcium-binding adaptor molecule
ID	Injected dose of radioactivity
IDIF	Image-derived input function
ISF	Interstitial fluid
K <sub>1</sub>	Rate constant of radioligand from plasma to tissue
LB	Lewy body
LDL	Low-density lipoprotein
LN	Lewy neurite

LTP	Long-term potentiation
MAO	Monoamine oxidase-B
MRI	Magnetic resonance imaging
MSA	Multiple system atrophy
NAC	Non-amyloid beta component
NeuN	Neuronal nuclear antigen
NMDA	N-methyl d-aspartate
PBS	Phosphate-buffered saline
P2X <sub>7</sub> R	Purinergic receptor P2X subunit 7
PD	Parkinson's disease
PET	Positron emission tomography
PS1	Presenilin 1
ROI	Region of interest
ROS	Reactive oxygen species
scFv	Single-chain variable fragment
SN	Substantia nigra
<i>SNCA</i>	Synuclein alpha gene
SNARE	Soluble N-ethylmaleimide-sensitive factor attachment protein receptor
SPECT	Single-photon emission computed tomography
SUV	Standardised uptake value
SV2A	Synaptic vesicle protein 2A
TAC	Time-activity curve
TBS	Tris-buffered saline
TBST	Tris-buffered saline with triton
TCM	Tissue compartmental model
TfR	Transferrin receptor
ThS/ThT	Thioflavin S/Thioflavin T
TLC	Thin-layer chromatography
TSPO	Translocator protein
VAMP2	Vesicle-associated membrane protein 2
V <sub>T</sub>	Volume of distribution
wt	Wild type

# Introduction

Positron emission tomography (PET) has been used widely for central nervous systems (CNS) diseases since the 1980s when Reivich and Kuhl first used a fluorine-18 ( $^{18}\text{F}$ ) radiolabelled glucose analogue,  $^{18}\text{F}$ -fluorodeoxyglucose (FDG), to measure cerebral blood volume in humans<sup>1</sup>. Nowadays, PET is a strongly embraced imaging technique for many neurodegenerative diseases, including Alzheimer's disease (AD) and Parkinson's disease (PD), by which the diseases can be diagnosed, and the progression can be followed based on different pathological features. Currently, PET ligands that bind to amyloids, synaptic proteins, receptors and enzymatic targets are used in clinics for AD and PD, while many other ligands are still under development. Developing a PET ligand targeting disease-specific proteins is a high priority as it enables early and accurate diagnosis and can help to evaluate treatment effects.

The roads to new radioligands are filled with excitement but also challenges.

## Neurodegenerative diseases

Neurodegenerative diseases are a group of disorders characterised by dysfunction, degeneration and ultimately death of specific neuronal cells in the brain. Although different diseases exhibit distinct hereditary and sporadic conditions, they share many common pathological features, such as aggregated proteins, dysregulated synapses, and neuroinflammation. AD and PD are the most common neurodegenerative diseases. The number of people affected is increasing each year, partly due to the increasing life span in the population but also attributed to improved methods to detect and diagnose diseases. Most AD and PD cases are idiopathic and uncommon among people younger than 50, making age the largest risk factor for developing the diseases<sup>2,3</sup>.

## Parkinson's diseases

PD was first described by James Parkinson in 1817<sup>4</sup>. The neuropathological characteristics of the disease were later defined as Lewy bodies and Lewy

neurites, prominently occurring in the substantia nigra (SN)<sup>5,6</sup>. Alpha-synuclein ( $\alpha$ Syn) was identified as a component of the Lewy body (LB) and Lewy neurite (LN) 180 years after the first PD description<sup>7,8</sup>. The discovery of  $\alpha$ Syn inclusions in LB and LN also linked PD to dementia with Lewy bodies (DLB) and multiple system atrophy (MSA)<sup>9,10</sup>. Recent studies suggest that early pathological changes in  $\alpha$ Syn occur in multiple tissues, such as the skin and colon, which could enable early and new diagnostic opportunities<sup>11,12</sup>.

Motor symptoms are the centre of clinical diagnostic criteria for PD<sup>13</sup>. Patients with PD can experience movement difficulties, including resting tremors, rigidity, akinesia, and posture imbalance<sup>14</sup>. They are also commonly affected by non-motor symptoms, including cognitive impairment, sleep disturbances, depression and loss of smell<sup>15</sup>. Magnetic resonance imaging (MRI) and dopaminergic neuroimaging sometimes corroborate in clinics to exclude PD because current imaging markers cannot distinguish PD from other disorders giving rise to parkinsonism.

The majority of PD cases arise in a sporadic form. However, studies of disease-causing genes provide valuable insights into disease mechanisms, diagnosis and treatment. Gene mutations linked to PD only account for 5-10% of the PD population<sup>16</sup>. Among many known genes linked to PD, point mutations and whole gene multiplications of the  $\alpha$ Syn encoding gene, *synuclein alpha (SNCA)*, have been confirmed to be associated with familial and sporadic PD<sup>8,17</sup>. The results also suggest that higher expression of wild-type  $\alpha$ Syn can trigger neurodegeneration<sup>8,18,19</sup>.

Gender differences in PD have been a topic receiving substantial attention for a long time. Although epidemiological data suggests that men have higher morbidity of PD, the risks of developing both motor and non-motor symptoms are higher in women once the disease has started<sup>20,21</sup>. The sex-related disease pattern also makes it more challenging to search for a common biomarker for routine clinical practice.

Unfortunately, no disease-modifying treatment exists for PD yet, but certain treatment strategies may provide relief of the symptoms. The most common medication for PD is still *Levodopa*, a drug that increases dopamine levels since low dopamine concentration is linked to parkinsonism<sup>22,23</sup>. On the positive side, many drug candidates are currently being studied in clinical trials, from dopamine receptor agonists to anti- $\alpha$ Syn aggregation therapies<sup>24</sup>, and the results from these studies will be revealed in the coming years.

## Alpha-synuclein

Alpha-synuclein is a 140 amino acid (aa) presynaptic protein predominantly expressed in the brain and enriched in presynaptic nerve terminals<sup>25-27</sup>. The protein consists of three regions: a positively charged N-terminal amphipathic region (aa 1-60), a hydrophobic mid-region containing the non-amyloid  $\beta$

component (NAC) domain (aa 61-95), and a negatively charged acidic C-terminus region (aa 96-140). The N-terminal region can associate with lipids, which can be attributed to the formation of  $\alpha$ -helices by the 11 aa repeats<sup>28</sup>. The mid-region was first discovered in plaques associated with AD and was particularly involved in conformational change and amyloid-like aggregation<sup>27,29,30</sup>. The C-terminal is proposed to contain protein-molecule interaction sites that interact with synaptic vesicles<sup>31</sup>, and is the site where the most post-translational modifications occur<sup>32</sup>.

The  $\alpha$ Syn protein has been reported to exhibit many functions at the synapse related to protein interaction, dopamine metabolism, neurotransmitter release and synaptic plasticity<sup>33,34</sup>. Alpha-synuclein binds to many proteins, mainly at the presynaptic terminal, including proteins of soluble N-ethylmaleimide-sensitive factor attachment protein receptor (SNARE) and dopamine transporter<sup>33,35</sup>. It can promote SNARE-complex assembly by cross-bridging SNARE vesicle-associated membrane protein 2 (VAMP-2), which is essential in synaptic vesicle docking in the exocytosis pathway<sup>33,36</sup>.

Further,  $\alpha$ Syn can impact dopamine metabolism. It can inhibit dopamine biosynthesis by reducing tyrosine hydroxylase activity and regulates the recycling pool of dopaminergic synaptic vesicles<sup>37-39</sup>. In addition,  $\alpha$ Syn is assumed to affect neurotransmitter release because of the presynaptic localisation and interaction with other synaptic vesicle proteins. Knocking out  $\alpha$ Syn can induce changes in synapse structure, size or synaptic protein expression<sup>33,40,41</sup>. Some studies indicate  $\alpha$ Syn enhance synaptic transmission and endocytosis in neurons<sup>42,43</sup>, whereas a decrease in neurotransmitter release or no effect has also been reported<sup>34,40,44</sup>. Inconsistent results from these studies suggest that  $\alpha$ Syn may not be responsible for neurotransmission and synaptic plasticity via direct action on the release machinery but rather play a role in the organisation of different synaptic vesicle pools in the pre-synapse<sup>38,45,46</sup>.

Alpha-synuclein is a natively unfolded protein with significant conformational plasticity<sup>47,48</sup>. The protein varies from a distinct secondary structure element to a wide range of high molecular weight assemblies and deposits as intracellular inclusions. The debate regarding the native form of the  $\alpha$ Syn structure in the disordered state has lasted for years with controversial results from different studies<sup>49,50</sup>. However, it is widely accepted that  $\alpha$ Syn aggregates are formed from soluble monomers via oligomeric intermediates, or protofibrils, into insoluble fibrils, which are composed of several protofilaments with a cross  $\beta$ -sheet structure<sup>51,52</sup> (Fig. 1).

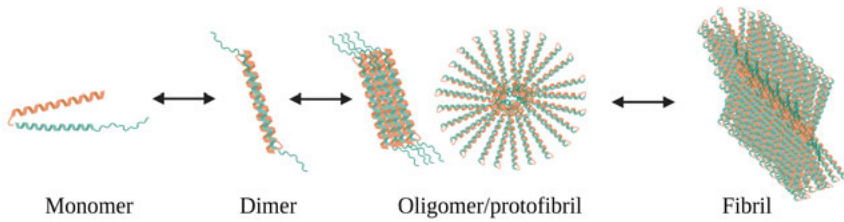


Fig. 1. Aggregation pathway for  $\alpha$ Syn. Monomeric proteins undertake conformation changes and subsequently aggregate to soluble oligomers and protofibrils, and later to larger insoluble fibrils.

Further, oligomers may represent the most toxic aggregation state of  $\alpha$ Syn<sup>53,54</sup>. Oligomers can affect multiple cellular pathways and lead to intracellular calcium dysregulation, mitochondrial abnormalities, and synaptic dysfunction<sup>55–57</sup>. Phosphorylation of  $\alpha$ Syn at the Ser-129 position can promote the accumulation of oligomeric  $\alpha$ Syn *in vitro* and accelerate the formation of  $\alpha$ Syn inclusions<sup>58,59</sup>.

## Alzheimer's disease

Psychiatrist and neuropathologist Alois Alzheimer first documented AD in 1901 and published his observations in 1906<sup>60</sup>. Two major neuropathological hallmarks characterise the disease: extracellular plaques composed of amyloid-beta ( $A\beta$ )<sup>61</sup> and intraneuronal fibrillary tangles consisting of abnormally phosphorylated tau protein<sup>62</sup>. Apart from plaques and tangles, inflammation<sup>63</sup>, axonal degeneration<sup>64</sup>, synapse and neuronal loss are also associated with AD pathology<sup>65,66</sup>. Subsequently, memory loss is usually the first sign of AD, but the pathological process starts decades earlier than the occurrence of cognitive symptoms. Accordingly, cognitive tests, diseases-related protein measurements in cerebrospinal fluid (CSF) and brain imaging are used in AD diagnosis<sup>67,68</sup>.

In general, women are more likely to develop AD than men considering women's overall longer life span<sup>69,70</sup>. Besides common risk factors such as apolipoprotein E (*APOE*) genotype, sex-specific risk factors differ in AD. One example of such a risk factor is depression. Depression was associated with a higher incidence of mild cognitive impairment (MCI) and probable dementia<sup>71</sup>. Compared to men, women who suffer from AD are twice as likely to develop depression, and the probability of dementia is significantly increased for women with a history of depression<sup>72</sup>.

For AD, cholinesterase enzyme inhibitors and antagonists to N-methyl d-aspartate (NMDA) receptor are current symptomatic treatments. In order to modify the underlying disease pathology and halt disease progression, most immunotherapies aim to eliminate  $A\beta$  aggregates from the brain by using anti-

A $\beta$  antibodies. After many failures, encouraging news came last year from phase III data of the anti-A $\beta$  monoclonal antibody, *Lecanemab*. It is an antibody with a higher affinity for soluble A $\beta$  protofibrils while having a slightly lower affinity for A $\beta$  fibrils, i.e. the main constituents of plaques. Patients who received the highest dose of *Lecanemab* (10 mg/kg bi-weekly) displayed a decrease in amyloid burden<sup>73</sup>. More importantly, cognitive decline in the treated group was 27% slower compared to the placebo group<sup>73</sup>. Also, the antibody *Aducanumab* has shown promising results in clinical trials, but its efficacy was limited in some studies and has been debated<sup>74</sup>.

## Amyloid-beta

The A $\beta$  peptide is a 39-43 aa peptide produced by cleavage of the transmembrane A $\beta$  precursor protein (APP), where APP is first cleaved by  $\beta$ -secretase, followed by  $\gamma$ -secretase<sup>75</sup>. The cleavage of APP can lead to different isoforms of A $\beta$ . A $\beta$ 40 and A $\beta$ 42 are the major forms of the A $\beta$  peptide in the brain, differing by a slight structural difference at the C-terminus, resulting in different aggregation characteristics. A $\beta$ 42 is more prone to aggregate than A $\beta$ 40<sup>76,77</sup>. A decreased A $\beta$ 42/A $\beta$ 40 ratio and reduced A $\beta$ 42 concentration in CSF are biomarkers used for AD diagnosis. Notably, these CSF biomarkers have unique trajectories during disease development. CSF A $\beta$ 42 and A $\beta$ 40 decline before brain amyloid can be detected by PET and reach a plateau when amyloid PET signals are still increasing<sup>78</sup>.

The A $\beta$  aggregation pathway is similar to  $\alpha$ Syn, starting with misfolded monomers that aggregate into soluble fibrils and eventually into insoluble fibrils and A $\beta$  plaques<sup>79</sup> (Fig. 1). The “amyloid cascade hypothesis” suggests that excessive A $\beta$  production and accumulation lead to progressive synaptic and neuronal injury, ending in widespread neuronal dysfunction and dementia<sup>80</sup>. The diffuse nature of soluble protofibrils makes it easier to interact with cell membranes that ultimately cause neuronal damage. Cells exposed to A $\beta$  protofibrils are associated with more oxidative damage by reactive oxygen species (ROS) generation and mitochondria dysfunction<sup>81-83</sup>. It can also disrupt cell membrane integrity by interfering with voltage-dependent Ca<sup>2+</sup> channel and NMDA receptors, causing abnormal Ca<sup>2+</sup> influx and inhibiting long-term potentiation (LTP)<sup>84,85</sup>.

## Ageing synapse

A synapse is a functional unit in the brain that passes information between neurons. The stability of the synapse depends on synaptic morphology and plasticity. During ageing, the reduction of presynaptic proteins, such as syn-

apoptophysin, is related to the overexpression of histone deacetylases<sup>86,87</sup>. Acetylation of synaptic active zone protein regulated by histone deacetylases has been found to promote synapse degradation, suggesting epigenetic factors play a role in modifying synaptic proteins in ageing<sup>87,88</sup>. Various groups reported different results regarding synaptic morphology in ageing. Both decreased and stable synapse numbers in the hippocampal and cortical regions have been described through ultrastructure studies<sup>89</sup>. The variance in sample size, brain regions and analytical methods may cause these controversial results<sup>90</sup>. Studies in nonhuman primates and rats have also proposed that changes in synaptic morphology are associated with brain regions and the shape type of spines<sup>91-93</sup>. In the group of dendritic spines, thin spine density is more altered in ageing compared to the mushroom spine as it forms smaller and weaker synapses<sup>92-94</sup>.

Throughout life, synaptic connections weaken or strengthen, causing changes in their functions to maintain neurotransmission. This process is also known as “synaptic plasticity”. Synaptic plasticity is crucial for cognitive functions such as learning and memory. Many studies have proved that impaired synaptic connectivity is one of the major neuropathological features in ageing and neurodegenerative diseases<sup>95</sup>. Compared to a widespread loss of neurons in neurodegenerative diseases, cognitive-impaired ageing is instead associated with a disturbance of synaptic plasticity<sup>96-98</sup>. Cognitive-impaired ageing has been linked to defects in LTP induction and maintenance<sup>99</sup>. In parallel to morphology, synaptic plasticity in regions involved in hippocampal and cortical circuits is most vulnerable to age-related change<sup>100</sup>.

## PET imaging of AD and PD

Functional imaging has been used in clinical routine, enabling pathology detection in small brain areas and tracking pathological changes<sup>78</sup>. Developing a PET radioligand to visualise amyloid is one of the major achievements in molecular imaging for diagnosing neurodegenerative diseases.

The first well-accepted amyloid PET radioligand was carbon-11 (<sup>11</sup>C) labelled Pittsburgh compound B, [<sup>11</sup>C]PiB<sup>101</sup>. Structurally, it is an analogue of thioflavin-T, a histological dye for staining  $\beta$ -sheet structures in aggregated proteins<sup>102</sup>. However, the short half-life of <sup>11</sup>C and the need for an on-site cyclotron hampers its broader use. After the successful synthesis of [<sup>11</sup>C]PiB, three fluorine-18 (<sup>18</sup>F) labelled compounds have been developed and approved by U.S. Food and Drug Administration (FDA), namely [<sup>18</sup>F]Florbetapir, [<sup>18</sup>F]Florbetaben and [<sup>18</sup>F]Flutemetamol<sup>103-106</sup>. While these radioligands have over 90% sensitivity and are used primarily to detect amyloid<sup>107</sup>, they bind to all  $\beta$ -sheet structures with similar nanomolar range affinities<sup>108,109</sup>. This makes them less specific for A $\beta$ , thus undermining the detection accuracy when patients have mixed pathologies. Also, amyloid PET signals saturate while the

disease still accelerates<sup>110,111</sup>, which is less optimal for longitudinal monitoring of disease progression. Moreover, [<sup>11</sup>C]PiB binding was reported to be very low in some gene mutation carriers, such as AD patients with Arctic *APP* mutation, as this mutation increases the amount of diffuse A $\beta$  aggregates while reducing the fibrillar A $\beta$  format<sup>112</sup>. Hence, developing a radioligand that can specifically bind to diffuse and soluble A $\beta$  aggregates or, even better, can distinguish different A $\beta$  species is still of great interest.

Besides amyloid PET, tau PET is believed to be a prognostic tool in AD as tau correlates better with AD severity than A $\beta$  and displays distinct spreading schemes in different neurodegenerative diseases<sup>113,114</sup>. The first approved tau PET ligand was [<sup>18</sup>F]flortaucipir<sup>115</sup>. Established tau PET ligands have high sensitivity to distinguish AD and non-AD neurodegenerative diseases<sup>116</sup>. Further, the signals strongly correlate with cognitive impairment in advanced AD and serve this purpose better than amyloid PET<sup>117–119</sup>. Still, current tau PET imaging is challenged by off-target binding and conserved ability to differentiate tau aggregates in non-AD tauopathies<sup>120,121</sup>.

Since PD is related to the loss of dopaminergic neurons, several radioligands targeting the dopaminergic system are available for PD diagnosis<sup>122</sup>. For example, [<sup>18</sup>F]fluoro-L-dopa can image L-aromatic amino-acid decarboxylase (AADC) activity for assessing the presynaptic dopaminergic pathway, while [<sup>18</sup>F]FE-PE2I that targets the dopamine transporter can measure the reuptake of dopamine from the synaptic cleft into the synapse<sup>123,124</sup>. Further, several ligands, such as [<sup>18</sup>F]fallypride, target dopamine receptors to evaluate receptor density. As for imaging of pathological proteins, however, no radioligand can directly visualise and quantify  $\alpha$ Syn in PD despite extensive efforts to develop such a radioligand<sup>125</sup>. One of the most promising PET radioligand candidates for  $\alpha$ Syn imaging developed by AC Immune was only able to visualise  $\alpha$ Syn in patients with MSA. This could be due to the lower amount of  $\alpha$ Syn in the PD brain compared to MSA and the different conformation of  $\alpha$ Syn aggregates in the two diseases<sup>126</sup>.

In addition, PET radioligands targeting immune factors such as translocator protein (TSPO) have been explored. Upregulated TSPO expression is found in reactive astrocytes and microglia, a pathological feature in AD and PD<sup>127</sup>. TSPO PET is used in clinics to monitor immunomodulatory therapies, although it lacks cellular specificity<sup>128</sup>. Other neuroinflammation markers such as monoamine oxidase-B (MAO-B) and purinergic receptor P2X<sub>7</sub>R are also used and investigated as PET targets<sup>129,130</sup>. The main challenge for PET imaging of neuroinflammation is the localisation of a distinct target, as neuroinflammation markers tend to be expressed in several cell types and modulated by different pathways.

As discussed previously, the density and functionality of synapses are essential for cognition, and changes in synaptic plasticity and transmission efficacy are strongly associated with AD and PD pathology. In AD, cognitive decline correlates better with synaptic dysfunction than extracellular plaque

load or tau<sup>96,131–133</sup>, suggesting synaptic loss is an earlier marker than cognitive impairment<sup>134,135</sup>. Thus, imaging of synaptic density is a rational strategy to estimate cognitive function and brain degeneration. Starting from [<sup>11</sup>C]UCB-J and its analogues<sup>136–138</sup>, a number of radioligands have been developed to directly visualise synaptic density through binding to synaptic vesicle glycoprotein 2A (SV2A)<sup>139–141</sup>. SV2A is ubiquitously and abundantly distributed in the human and mouse brain<sup>142,143</sup>. [<sup>11</sup>C]UCB-J PET studies have linked neurodegeneration with loss of synaptic density in humans and animals<sup>137,144–148</sup>. AD patients displayed an approximate 40% reduction in radioligand binding compared with healthy controls<sup>144</sup>. Also, the binding of [<sup>11</sup>C]UCB-J in substantia nigra in early PD patients was significantly lower than in the control group<sup>145,149</sup>. In combination with other biomarkers, imaging of synaptic density could be especially useful in drug development, both in the preclinical setting when testing new compounds in animal models and later in the clinical trials of candidate drugs.

Recently, studies used [<sup>11</sup>C]UCB-J PET to investigate if the method could reveal synaptic density changes during ageing<sup>150–152</sup>. Two studies in human subjects suggested unaltered [<sup>11</sup>C]UCB-J retention during ageing after accounting for brain atrophy<sup>150,151</sup>. This confirms the histological findings that synaptic density is relatively stable during healthy ageing. Andersen et al. (2022) also measured the glucose metabolism by [<sup>18</sup>F]FDG and reported that the change in glucose metabolism was not consistent with [<sup>11</sup>C]UCB-J alteration in the same brain region. Hence, the different patterns of synaptic density and glucose metabolism during ageing indicate that several mechanisms are involved in healthy ageing<sup>150</sup>.

## Antibody PET

### **The blood-brain barrier (BBB)**

The BBB separates the brain from the systemic circulation. It is a highly regulated microenvironment that maintains brain homeostasis. Physiologically, the BBB shields the brain from toxic substances originating from the periphery and filters harmful compounds from the brain back to blood circulation. Local impairment of the BBB can exist in the brain during pathological conditions, such as neurodegenerative- and inflammation-related diseases<sup>153,154</sup>.

The BBB is composed of a microvascular endothelium, astrocytes, basement membrane, pericytes and neurons<sup>155</sup> (Fig. 2). The brain microvascular endothelial cells have distinctive functions, including the responsibility for composing and regulating tight junctions<sup>156</sup>. Astrocytes and pericytes support the endothelial cells for proper function and integrity<sup>157,158</sup>. Neurons can modulate BBB permeability and produce unique enzymes<sup>159,160</sup>.

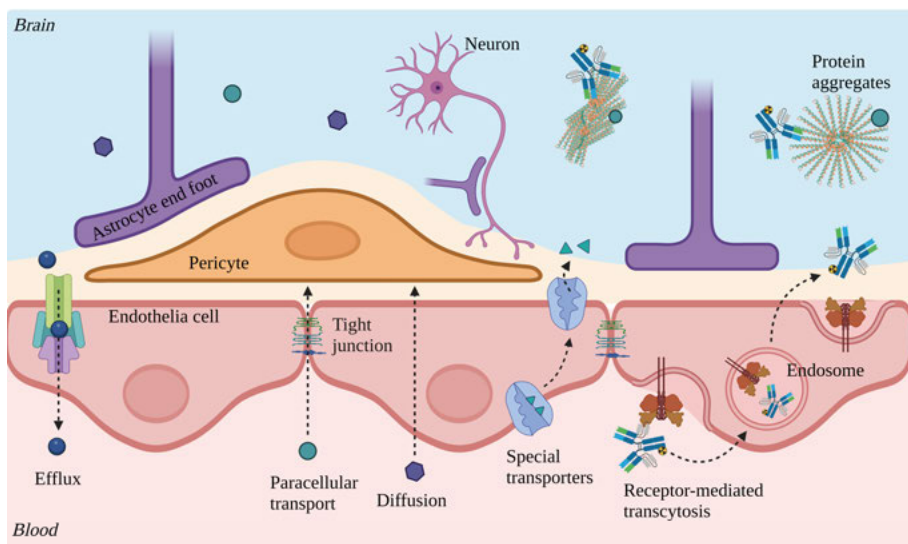


Fig. 2. Illustration of the BBB and molecule passage through it.

Tight junctions that connect the endothelial cells of the BBB are the main elements for restricting paracellular transport. Consequently, the BBB only allows small hydrophilic molecules to pass into the brain by paracellular transport. Lipophilic molecules < 400-500 Da may pass through the BBB by passive diffusion, while glucose and amino acids can enter the brain via specialised transporters. Large molecules, such as peptides and proteins, need to pass through the BBB by receptor-mediated transcytosis or charge-dependent absorptive transcytosis. Receptor-mediated transcytosis at the BBB is essential for the brain delivery of ligands such as transferrin, insulin, and low-density lipoprotein (LDL)<sup>161</sup>. Low BBB permeability is a concern when developing new drugs for brain disorders<sup>162</sup>. Very low amounts of PET radioligands for CNS targets are usually administered, commonly referred to as “tracer dose”. In line with this, the radioligands should be based on molecules with excellent BBB permeability to reach the brain parenchyma sufficiently.

### Bispecific antibodies

By far, the majority of PET radioligands are based on small “drug-like” molecules. Although small molecules with characteristics such as high lipophilicity can pass the BBB, they often exhibit high unspecific binding in the lipophilic environment of the brain. In addition, some small molecules developed for imaging of specific protein aggregates exhibit cross-reactivity to other pathological proteins<sup>163,164</sup>. For example, most molecules developed as PET radioligands for imaging  $\alpha$ Syn deposits also bind to the  $\beta$ -sheet structure of the  $A\beta$  fibrils, which are also seen in the PD with dementia and DLB brains<sup>165,166</sup>.

Antibodies have long been explored as PET radioligands to avoid off-target and unspecific binding in oncology<sup>167</sup>. Despite being highly specific for their target, antibodies have not been considered as CNS radioligands because of their low uptake in the brain<sup>168</sup>. Various mechanisms such as utilising endogenous transport(er) systems and focused ultrasound have been explored to enhance brain uptake for large molecules<sup>169–172</sup>. Among them, the transferrin receptor (TfR) transcytosis system with bispecific antibody constructs that bind both a primary brain target and the TfR on brain endothelial cells has proved to be a promising strategy to facilitate brain delivery via receptor-mediated transcytosis<sup>173–175</sup>. Several radiolabelled bispecific antibodies targeting A $\beta$  and TfR have been described and tested *in vivo*<sup>176–179</sup>. In these studies, the rat anti-mouse TfR binding antibody, 8D3<sup>180,181</sup>, was fused to antibodies against A $\beta$  to generate bispecific antibody constructs. The bispecific antibodies displayed greater brain uptake (up to 80-fold) than their corresponding unmodified IgG antibody format and, when radiolabelled, successfully detected A $\beta$  in transgenic mouse brains<sup>176,178</sup>. Thus, engineered antibodies are becoming a new possibility for brain imaging and novel treatments of neurodegenerative disease<sup>182–184</sup>. However, several challenges remain before antibody-based PET can be translated to applications in the human brain. First, the homology of the TfR sequence between rodents and humans is around 90%. This hampers the direct translation of PET radioligand candidates from mouse to human, although antibodies binding to the human TfR exist<sup>185</sup>. Second, the weeks- or months-long biological half-life of IgG antibodies does not match the minutes- or hours-long radioactive half-life of commonly used radionuclides in PET. When imaging the brain, long circulation of radiolabelled antibodies will contribute to the background signal from the blood, thus masking the brain-derived signals.

Studies using antibody fragments instead of full-sized IgGs as PET radioligands to accelerate elimination are ongoing<sup>177,186</sup>. Meanwhile, the concept of “pretargeted imaging” using biorthogonal click chemistry in the CNS can also help to postpone the injection of radioactivity, enabling PET scans later when systemic and unbound antibody has been cleared<sup>187</sup>. Pretargeted imaging is based on the administration of antibodies prior to the administration of a small molecule carrying the radioactive label. The two components, antibody and small molecule, will conjugate in the body, allowing the usage of short-lived radionuclides<sup>188</sup>. For some targets, such as  $\alpha$ Syn, the third challenge comes from the intracellular location and low target density. Most of the  $\alpha$ Syn aggregates are located inside the cell, while little is present in extracellular space<sup>7,189</sup>. Therefore, antibodies do not only need to cross the BBB but also have to pass the cell membrane to interact with the target.

## Quantification of dynamic PET images

Kinetic modelling is a tool to estimate and quantify the pharmacokinetics of a radioligand in dynamic PET studies. Kinetic modelling strives to assess various factors for mathematical analysis of the dynamic processes of a radioligand in a specific time course. The brain, blood, and other intravascular components can be considered as different compartments into which the radioligand can distribute<sup>190</sup>. In order to describe the dynamic processes of the radioligand in a complete model, including perfusion, specific binding, and non-specific binding, several equations that describe the radioligand concentration in each compartment over time can be used simultaneously to estimate these parameters. However, depending on the radioligand used, one or two key parameters most often correlate with the property under investigation. For example, the brain-to-blood concentration ratio (the distribution volume  $V_T$  in PET nomenclature) is often calculated as an estimate of total brain delivery<sup>191</sup>. Many models thus require the measurement of radioligand concentrations in both blood (blood sampling) and brain (PET).

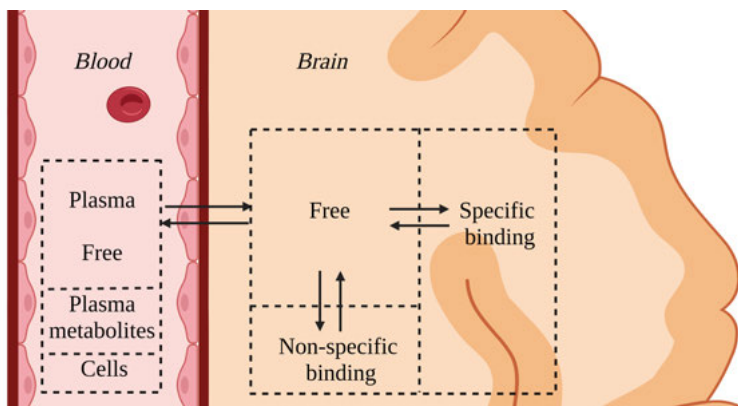


Fig. 3. Model describing radioligand behaviour in blood and brain. In the blood, only free radioligand in plasma is available for brain delivery, although total plasma concentrations are usually used as an input. In the brain, radioligand can exist in unbound form (free) and bound forms (specific binding and non-specific binding).

If a region is devoid of the target (or if the target in the region is unaltered), it can usually be considered a “reference tissue”<sup>192</sup>. In such cases, using a reference model to estimate binding properties without plasma or blood input is possible, which means that blood sampling may be unnecessary. Reference tissue-based methods are appreciated, especially when working with small animals, as the small blood volume in rodents makes frequent blood sampling challenging.

For the same reason, using image-derived input function (IDIF) constitutes an attractive non-invasive alternative to arterial sampling in small animal PET. Several regions, such as the heart, vena cava and femoral arterial, have been

validated in rodents as a site from where the IDIF can be extracted<sup>193–196</sup>. However, the small organ size in rodents requires a PET and CT/MRI scanner with high spatial resolution. Moreover, partial volume effects, including both spill-in (higher radioactivity concentration surrounding the region-of-interest) and spill-out effect (lower radioactivity concentration in the surrounding region-of-interest), heavily influence the use of IDIF in rodents<sup>197</sup>. Partial volume effects will either overestimate or underestimate the true IDIF radioactivity<sup>198</sup>. Correcting the IDIF with *in vitro* analysis of blood samples is preferable to overcome the artefacts introduced by the IDIF application. Moreover, generating a population-based input curve can reduce the variation of IDIFs obtained from single animals. It can also help to obtain a good and robust estimation of radioligand brain retention<sup>197</sup>.

# Methodology

## Animal models

Four mouse models of AD and PD pathology were used in the thesis (Table 1). Transgenic mouse models Thy-1  $\alpha$ Syn (L61) and (Thy-1)-h[A30P] (A30P) lines were used to study  $\alpha$ Syn-induced PD pathology<sup>199,200</sup>. Moreover, transgenic tg-ArcSwe and A $\beta$  precursor protein gene *APP* knock-in mouse model, *App*<sup>NL-G-F</sup>, were used to study A $\beta$ -related pathology<sup>201,202</sup>.

Table 1. Research mouse models used in the thesis.

Model Name	L61	A30P	tg-ArcSwe	<i>App</i> <sup>NL-G-F</sup>
Background	(C57BL/6 $\times$ DBA/2)	C57BL/6	C57BL/6	C57BL/6
Allele pairs	heterozygous	homozygous	heterozygous	homozygous
Modification	SNCA: transgenic	SNCA: transgenic	APP: transgenic	APP: knock-in
Mutations	-	A30P	Swe, Arc	Swe, Arc, Ibe
Used in study	Paper I, III	Paper III	Paper I, II, V	Paper IV

Heterozygous transgenic L61 model mice overexpressing human wild-type  $\alpha$ Syn maintained on a C57BL/6  $\times$  DBA/2 background and age-matched non-transgenic wild-type controls (referred to as wt-L61 in **Paper I**) were used in **Paper I** and **III**. The L61 model reproduces several features of sporadic PD and has been well-characterised in several studies<sup>200,203–205</sup>.

L61 mice display a robust amount of  $\alpha$ Syn already at 2-3 months of age, and the brain concentration of  $\alpha$ Syn increases dramatically with age<sup>203,205</sup>. High pathology accumulation is observed in the thalamus, basal ganglia, substantia nigra, brainstem, hippocampus and cortex<sup>200,203,206</sup>. Some studies have reported a reduction of striatal dopamine and dopamine transporter in L61 mice<sup>204,207</sup>. However, like most other PD models, L61 do not mimic the loss of dopaminergic neurons observed in PD patients<sup>203</sup>. Still, L61 mice develop motor impairments such as hind limb claspings, and this behaviour worsens progressively with age, especially in males<sup>203,205,208</sup>. Moreover, compared to non-transgenic mice, loss of cortical and hippocampal CA3 neurons together with degeneration of presynaptic terminals has been reported in L61 mice<sup>207,209</sup>.

A30P mice overexpressing human  $\alpha$ Syn with the A30P-mutation under the Thy-1 promoter on a C57BL/6 background were also used in **Paper III**. A30P mice exhibit loss of dopaminergic neurons, possibly due to the mutant A30P  $\alpha$ Syn expression, which has a stronger effect than wt  $\alpha$ Syn on several pathways related to neuronal development and synaptic signalling<sup>210-212</sup>.

Two AD mouse models were used to study A $\beta$ -related pathology. The transgenic heterozygous mouse model tg-ArcSwe is maintained on a C57BL/6 background and overexpresses the human *APP* gene with the Arctic (E693G) and Swedish (KM670/671NL) mutations under the murine Thy-1 promoter. The concentration of soluble A $\beta$  protofibrils is elevated at one month of age<sup>201</sup>. The model develops dense-core amyloid plaques that are detectable when mice are five to six months old, followed by a higher A $\beta$  burden with increasing age<sup>201,213</sup>. Development of plaque pathology is initiated in the cerebral cortex, hippocampus and thalamus, and spreads to the whole brain at later stages of pathology progression<sup>201,214</sup>. However, detailed information about neuronal loss and synaptic dysfunction in this model is lacking. We used tg-ArcSwe and age-matched littermate wild-type control mice (in **Paper I**, referred to as wt-ArcSwe) to study synaptic dysfunction related to A $\beta$  pathology. In addition, wild-type mice of C57BL/6 background were also used in **Paper II** to investigate a potential age-related difference of SV2A PET imaging and in **Paper IV** to study the delivery of bispecific antibodies to the brain with microdialysis. In **Paper V**, tg-ArcSwe mice were used to study if antibody treatment can block the binding of amyloid radioligands rather than decrease A $\beta$  pathology and, in this way, reduce the PET signals.

*APP* knock-in mouse model of AD, *App*<sup>NL-G-F</sup>, with the Swedish (Swe, “NL”), Arctic (Arc, “G”), and Iberian (Ibe, “F”) mutations was used in **Paper IV**. Even without overexpression of APP, the three mutations result in an early onset of A $\beta$  deposition in *App*<sup>NL-G-F</sup> brain tissue starting at 2 months, displaying an increasing amount of total A $\beta$  and A $\beta$ 42/A $\beta$ 40 ratio. The fast aggregation of A $\beta$  continuously increase total brain A $\beta$  levels with age, leading to synaptic alteration and memory deficiency<sup>202</sup>.

## Establishment of an $\alpha$ Syn deposition model

The present thesis also includes establishing an  $\alpha$ Syn deposition mouse model used in **Paper III**. The deposition model is a straightforward method to test radioligand binding to  $\alpha$ Syn *in vivo*.

In short, wt-L61 mice were placed under anaesthesia with isoflurane and fixed in a stereotactic frame. After local analgesia and skull exposure, the stereotactic frame was attached to a microsyringe and set to the correct coordinates to provide an accurate position for the injection site. A hole was drilled in the skull at the injection site, leaving the dura intact. Then, PBS or  $\alpha$ Syn fibrils generated from recombinant human  $\alpha$ Syn monomers were slowly injected into the dorsal striatum (Fig. 4). The presence of fibrils was verified by immunohistochemistry staining and amyloid PET.

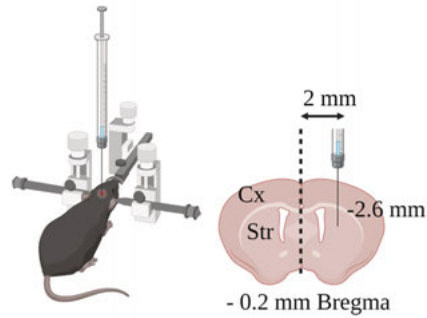


Fig. 4. Description of fibril deposition surgery. Cx: cortex. Str: striatum.

## Antibodies

Anti- $\alpha$ Syn and anti-A $\beta$  antibodies used in the thesis are listed in Table 2.

Table 2. Antibodies used in the thesis.

	<b>Bispecific antibodies</b>	<b>Unmodified format (IgG)</b>
Used in study	~ 210 kDa	~ 150 kDa
Paper III (anti- $\alpha$ Syn)	RmAb48-scFv8D3 RmAbSynO2-scFv8D3 RmAb38E2-scFv8D3 RmAb38F-scFv8D3 RmAb15-scFv8D3	RmAb48 <sup>217</sup> RmAbSynO2 <sup>218</sup> RmAb38E2 <sup>211</sup> RmAb38F <sup>211</sup> RmAb15 <sup>211</sup>
Paper IV (anti-A $\beta$ )	RmAb3D6-scFv8D3	RmAb3D6 <sup>168</sup>
Paper V (anti-A $\beta$ )		RmAb158 <sup>219</sup>

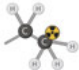

In **Paper III** and **IV**, both bispecific and IgG formats of antibodies were produced for comparison. As previously described, the bispecific antibodies are generated by fusing the C-terminal end of the light chain of an IgG2c backbone to a single-chain variable fragment of the rat anti-mouse TfR antibody

8D3 (scFv-8D3)<sup>180</sup>. The scFv-8D3 domain dramatically increases brain uptake of the antibody through TfR-mediated transcytosis<sup>179,215</sup>. To mimic the clinical studies of *Lecanemab*, mAb158, the murine parent version of *Lecanemab*, was used at a high dose of 50 mg/kg to treat transgenic animals in **Paper V**. For antibody production, the DNA sequences encoding the antibodies were cloned into a pcDN3.4 vector. Plasmid DNA was then amplified in *E. coli* (Top10) cells and transfected to the human Expi293 cells. The cells were incubated for approximately one week before harvesting and purified by an ÄKTA protein purification system with a protein G column<sup>216</sup>.

## Radiolabelling

Radioligands used for each study are listed in Table 3. <sup>18</sup>F, <sup>11</sup>C and tritium (<sup>3</sup>H) were used to label small molecule radioligands, while iodine-125 (<sup>125</sup>I) and iodine-124 (<sup>124</sup>I) were used for radiolabelling antibodies.

Table 3. Radioligands used in the thesis.

Small molecules		Antibodies	
			
Paper I	[ <sup>11</sup> C]UCB-J	Paper III	[ <sup>125</sup> I]RmAbs*
Paper II	[ <sup>18</sup> F]SynVesT-1		[ <sup>124</sup> I]RmAb48-scFv8D3
	[ <sup>3</sup> H]UCB-J		[ <sup>124</sup> I]RmAbSynO2-scFv8D3
Paper III, V	[ <sup>11</sup> C]PiB	Paper IV	[ <sup>125</sup> I]RmAb3D6
			[ <sup>125</sup> I]RmAb3D6-scFv8D3

\* All anti- $\alpha$ Syn antibodies are given in Table 2.

Radionuclides <sup>18</sup>F and <sup>11</sup>C are the two most commonly used radionuclides for PET imaging, especially in the clinical setting. The main advantage of these two radionuclides is their pure positron ( $\beta^+$ ) emission (> 96% for both) during decay. This reduces the noise detected by PET, and further, it decreases the required amount of injected radioactivity and leads to less radioactivity exposure for the subject under investigation. It is crucial to keep the injected mass of the radioligand low when performing PET experiments to avoid eliciting a pharmacological effect while allowing for enough radioactivity for PET-based quantification and visualisation<sup>220</sup>. Besides suitable half-lives (109.8 min for <sup>18</sup>F and 20.4 min for <sup>11</sup>C)<sup>221</sup> for PET investigations that commonly include data collection during an hour, the short positron range of <sup>18</sup>F and <sup>11</sup>C due to their low endpoint energy contributes to high spatial resolution when detected by the PET scanner. This is especially important for PET imaging in rodents with a limited brain size<sup>222</sup>.

The half-life of  $^3\text{H}$  is 12.3 years, and it undergoes beta minus ( $\beta^-$ ) decay, emitting electrons that can only travel a small distance through the air (around 6 mm)<sup>221</sup>. Thus,  $^3\text{H}$ -labelled ligands cannot be used in PET imaging. Nevertheless, since hydrogen exists in nearly all organic compounds, this isotope of hydrogen is abundantly used in biological research.

Radionuclide  $^{125}\text{I}$  decays by 100 % electron capture (EC) to an excited state of tellurium-125 ( $^{125}\text{Te}$ ), which immediately decays by gamma emission of maximum energy of 35 keV into the ground state  $^{125}\text{Te}$ . The low energy of the photons limits the use of  $^{125}\text{I}$  in PET imaging. Still, the relatively long half-life (59.5 days) facilitates the detection of  $^{125}\text{I}$ -labelled compounds in single-photon emission computed tomography (SPECT) imaging and other gamma-counting related radioimmunoassays during an extended period after injection<sup>221</sup>.

$^{124}\text{I}$  is also a  $\beta^+$  emission nuclide with a half-life of 4.2 days<sup>221</sup>. Although the radionuclide has a complex decay scheme with only 23 %  $\beta^+$  emission decay of relatively high energies<sup>223</sup>, data correction by modern PET scanners allows for its use in PET with radioligands associated with slow pharmacokinetics, such as antibodies.

In the thesis, SV2A PET ligand [ $^{11}\text{C}$ ]UCB-J was used in **Paper I** to estimate synaptic density<sup>224</sup>. In **Paper II**, we used another SV2A radioligand, [ $^{18}\text{F}$ ]SynVesT-1<sup>225</sup>. The two compounds based on pyrrolidinone pharmacophore display similar affinity and specificity to SV2A<sup>226</sup> (Fig. 5), but  $^{18}\text{F}$  enables multiple scans per production.

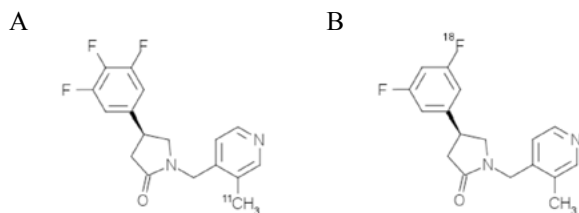


Fig. 5. Chemical structures of [ $^{11}\text{C}$ ]UCB-J (A) and [ $^{18}\text{F}$ ]SynVesT-1 (B).

Additionally, amyloid PET radioligand [ $^{11}\text{C}$ ]PiB<sup>101</sup> was used in **Paper III** to image and confirm fibril-like structures after intracranial deposition of  $\alpha\text{Syn}$ , and in **Paper V** to assess if the [ $^{11}\text{C}$ ]PiB signal was changed due to antibody binding to  $\text{A}\beta$  deposits. The three ligands were synthesised and produced in the PET centre at Uppsala University Hospital. [ $^3\text{H}$ ]UCB-J was commercially available (Novandi Chemistry AB, Sweden).

Antibodies were radiolabelled with  $^{125}\text{I}$  and  $^{124}\text{I}$  (PerkinElmer, The Netherlands) in **Paper III** and **Paper IV** using the Chloramine-T method, which oxidises the radioiodide ion to radioiodine by enabling electrophilic attack of the phenolic ring of tyrosine residues on the target antibodies<sup>227</sup>. The addition of

the reducing agent sodium metabisulphite was used to stop the iodination reaction. The labelled antibody was purified and isolated with size-exclusion chromatography cartridges (NAP-5).

## Autoradiography

Autoradiography is a common method for determining the spatial distribution of a radioligand and, thereby, the distribution of its target on brain tissue sections. Once the target density ( $B_{\max}$ ) is known, autoradiography can be used to determine the distribution, affinity, and selectivity of radioligand binding to the target. Both *in vitro* and *ex vivo* autoradiography was used in **Papers II-V**. Table 4 shows the purpose of using different autoradiography methods in the papers.

Table 4. Aims of autoradiography used in different papers.

	<i>In vitro</i> autoradiography	<i>Ex vivo</i> autoradiography
Paper II	To determine age-related changes in the $B_{\max}$ of SV2A	-
Paper III	To determine specificity and selectivity of [ $^{125}\text{I}$ ]RmAbs on mouse and human brain tissue	To confirm successful intracranial deposition of $\alpha\text{Syn}$ fibrils
Paper IV	-	To compare the brain distribution of a bispecific antibody to its unmodified format
Paper V	-	To compare [ $^{11}\text{C}$ ]PiB binding after PBS and antibody administration

*In vitro* autoradiography is carried out by applying an excessive amount of the radioligand directly on tissue sections, which allows the radioligand to bind to all potential targets, including both intracellular and extracellular targets, circumventing uptake limitation caused by the BBB and cell membranes. After washing, the sections are exposed to a phosphor imaging plate.

Compared to *in vitro* autoradiography, *ex vivo* autoradiography relies on exposing cryosections prepared from brains isolated from radioligand administered mice directly to a phosphor imaging plate.

When combined with immunohistochemical staining of tissue markers, the origin of radioactivity detected by autoradiography can be confirmed. For example, in **Paper III**, we showed that the radioactivity detected by *ex vivo* autoradiography originated from  $\alpha\text{Syn}$  fibril deposition.

## PET/CT imaging

PET is based on detecting compounds labelled with radioactive radionuclides that predominately decay by positron emission (also known as  $\beta^+$  decay). In the tissue, the positron collides with an electron and annihilates, emitting two gamma-ray photons (511 keV each) sent out in opposite directions. Within the PET scanner, the annihilation photons will be detected to determine the origin of the annihilation event, and with this information, 3D images can be created<sup>228,229</sup>. Regions showing high intensity in PET images represent the location of a large number of annihilation events, i.e. where the radioligand is abundant. PET images are often fused with CT or MRI to combine functional and anatomical imaging information<sup>230</sup>.

In **Paper I**, both transgenic and wild-type animals from the tg-ArcSwe and L61 models underwent 60 min dynamic PET scans with [<sup>11</sup>C]UCB-J and a 3-min CT scan in a Triumph<sup>®</sup>II PET/SPECT/CT scanner (TriFoil Imaging, Inc., Field of View (FOV) = 8.0 cm). In **Paper II**, a recently described radioligand targeting SV2A, [<sup>18</sup>F]SynVesT-1, was used to investigate potential changes in synaptic density during ageing in C57BL/6 mice. In the study, animals were PET scanned for either 90 min or 60 min using a nanoScan<sup>®</sup> PET/MRI 3T scanner (Mediso, Medical Imaging Systems, Field of View (FOV) = 10 cm) followed by a CT obtained in a nanoScan<sup>®</sup> SPECT/CT scanner. In **Paper III**, *in vivo* PET imaging was first conducted with [<sup>11</sup>C]PiB, a ligand bound to all forms of amyloid, which helped to verify the position of the injected  $\alpha$ Syn fibrils in the deposition model. Further, tg-L61, A30P and wt-L61 were scanned with [<sup>124</sup>I]RmAbSynO2-scFv8D3 and [<sup>124</sup>I]RmAb48-scFv8D3 in an attempt to visualise endogenously expressed  $\alpha$ Syn pathology.

PET images based on summed decay events within time frames of varying lengths during the 60 or 90 min scan were reconstructed and co-registered with the help of individual CT images to a standardised MRI-based atlas of the C57BL/6 mouse brain<sup>231</sup>. Selected brain regions were outlined based on the atlas to produce regions of interest (ROIs) that were applied to the dynamic set of PET images to generate regional time activity curves (TACs). Radioligand concentration in these ROIs was quantified either as a percentage of injected dose per gram tissue (%ID/g) (Eq. 1) or by weight normalised standardised uptake values (SUV) (Eq. 2).

$$\%ID/g = \frac{C_{img}(t)}{ID} \times 100\% \quad \text{Eq. 1}$$

$$SUV = \frac{C_{img}(t)}{ID/BW} \quad \text{Eq. 2}$$

Eq. 1 and Eq. 2 show the determination of %ID/g and SUVs (g/mL) at time t, respectively.  $C_{img}$  is the radioactivity measured in the ROIs, ID represents the injected dose of radioactivity, and BW represents animal body weight.

## Kinetic analysis of radioligand binding

The method to prepare data for subsequent kinetic analysis of radioligand binding in **Paper I** and **II** was based on previous publications<sup>195,196</sup>. We used an IDIF to substitute blood sampling during the PET scan. The blood IDIF was obtained by manually drawing an ellipsoid ROI (1.3 mm × 1.3 mm × 1.3 mm) in the left ventricle of the heart based on CT and the first two frames of PET images. Although the accuracy of this method can be debated, it provides a fast and fairly easy approach. It allows for a reliable comparison between individual animals and offers a practical alternative when blood sampling is not feasible.

In **Paper I** and **II**, several kinetic models were investigated and applied to the data, namely a one-tissue compartmental model (1TCM), a two-tissue compartmental model (2TCM), and the Logan plot with blood input. We focused on the two macro parameters: volume of distribution ( $V_T$ , ml/cm<sup>3</sup>) and the rate constant describing the delivery rate of the radioligand to the brain ( $K_1$ , ml/(cm<sup>3</sup>×min) as they are more stable than individual rate constants<sup>190</sup> (Fig. 6 and Table 5).

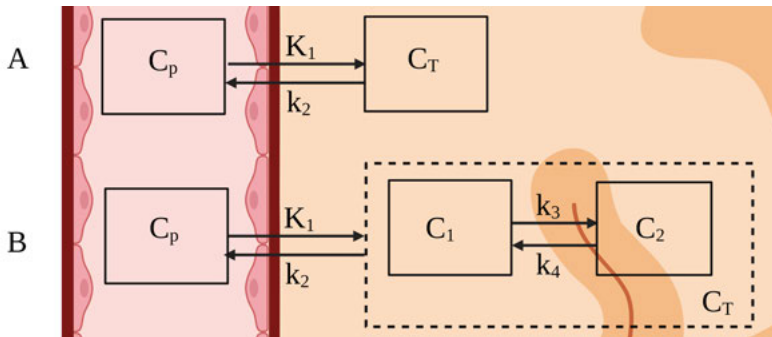


Fig. 6. Diagram of 1TCM (A) and 2TCM (B).  $C_p$  is the radioligand concentration in plasma (or blood), and  $C_T$  is the radioligand concentration in the tissue.  $K_1$  is the rate constant describing radioligand delivery from plasma to tissue, whereas  $k_2$  is the efflux coefficient from tissue to blood. Based on 1TCM, the concentration of tissue compartment ( $C_T$ ) is considered the sum of  $C_1$  and  $C_2$ .  $C_1$  represents the radioligand concentration not specifically bound to the target, and  $C_2$  represents the radioligand concentration that specifically binds to the target. Rate constants  $k_3$  and  $k_4$  signify the input and output rate coefficients between the two compartments, respectively.

The 1TCM is the simplest compartmental model with only two compartments and two rate constant parameters (Fig. 6A). The first compartment is the plasma or blood compartment used to derive the “input function”, which is an equation describing the radioligand concentration in blood or plasma ( $C_p$ ) over time. The second compartment describes the radioligand in tissue. The concentration in the tissue ( $C_T$ ) depends on radioligand concentration in plasma, influx, and outflow rates. Together,  $C_p$  and  $C_T$  determine  $V_T$  (Eq. 3).

$$V_T = \frac{C_T}{C_P} \quad \text{Eq. 3}$$

The 1TCM is not always sufficient for describing tissue distribution, and it may therefore be expanded to a model that includes a higher number of compartments, e.g. the 2TCM (Fig. 6B). Besides the blood compartment, the tissue compartment is divided into two compartments. The first tissue compartment describes free and nonspecific radioligand binding, while the second describes the radioligand that specifically binds to the target in the tissue.

Independent of any particular model structure, graphical analysis methods have been developed to obtain quantitative estimates of radioligand uptake. The Logan plot is a robust linear graphical analysis method to estimate the brain-to-blood distribution of a PET ligand. Because the  $V_T$  is decided based on the linear phase of the graph (Fig. 7), visual control of the linearity of the plots is important when using this method<sup>232-234</sup>. All important parameters in 1TCM, 2TCM and Logan plot are shown in Table 5.

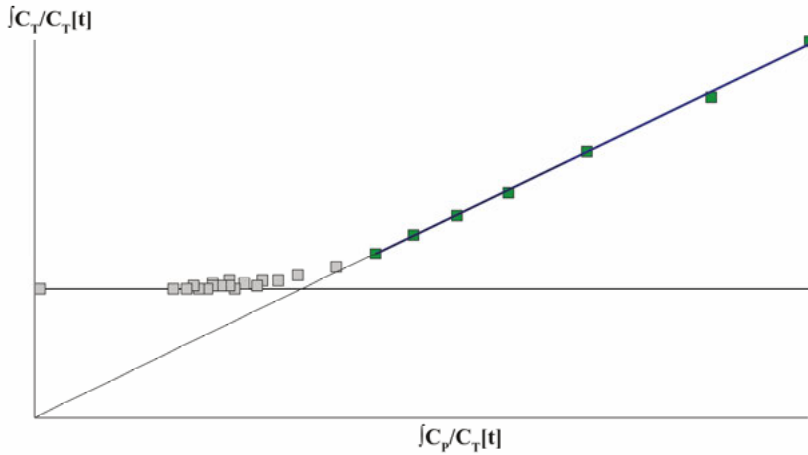


Fig. 7. Simplified graphical analysis of [<sup>11</sup>C]UCB-J time-activity data using the Logan plot based on blood input. The data used to estimate the linear phase (blue line) are indicated as green squares. Unused data is marked in grey.  $C_P$  is the plasma concentration of the radioligand (Bq/ml).  $C_T$  is the radioligand concentration (Bq/ml) in the region of interest.

In **Paper I**, we also calculated the model-independent ratio of the area under the TACs in brain and blood ( $AUC_{\text{brain/blood}}$ ) as a substitute for  $V_T$  (Eq. 4).

$$AUC_{\text{brain/blood}} = \frac{AUC_{\text{brain region}}}{AUC_{\text{blood}}} \quad \text{Eq. 4}$$

Table 5. List of important outcome parameters in kinetic modelling

Parameters	Estimated models	Meaning
$K_1$	1TCM, 2TCM	Unidirectional transport of the radioligand from the plasma or blood compartment to the first tissue compartment
$k_2$	1TCM, 2TCM	Rate constant describing the unidirectional transport back from tissue to the blood
$V_T$	1TCM, 2TCM, Logan plot	The ratio of the radioligand concentration in tissue to total concentration in plasma at equilibrium
$k_3$	2TCM	The association rate constant of the ligand with the specific binding sites
$k_4$	2TCM	The dissociation rate constant of the target-radioligand complex

Note: the same parameters have different equations in different models.

## Microdialysis

Microdialysis is an *in vivo* method that allows for continuous measurement of free, unbound analytes. It can quantify antibody concentration in the interstitial fluid (ISF) and provide information about the brain pharmacokinetics of administrated antibodies. So far, microdialysis has mainly been used to investigate small molecular drugs, but recently also to successfully measure and screen potential TfR-binding antibody candidates<sup>235–237</sup>. The microdialysis probe implanted into the target brain tissue of the animal is a small “Y” shaped catheter containing an inlet and outlet port with a semi-permeable membrane located at the bottom tip (Fig. 8A). The membrane has a large molecular weight cut-off at 3 MDa that allows extracellular molecules to diffuse into the perfusate. The perfusate in the syringe mimics the extracellular fluid and is slowly pumped through the inlet port to the membrane. The dialysate then carries solutes out from the outlet port (Fig. 8B). Dialysate is collected for neurochemical analysis, and the target chemical in the dialysate is called an analyte. In our case, it is the antibody under investigation.

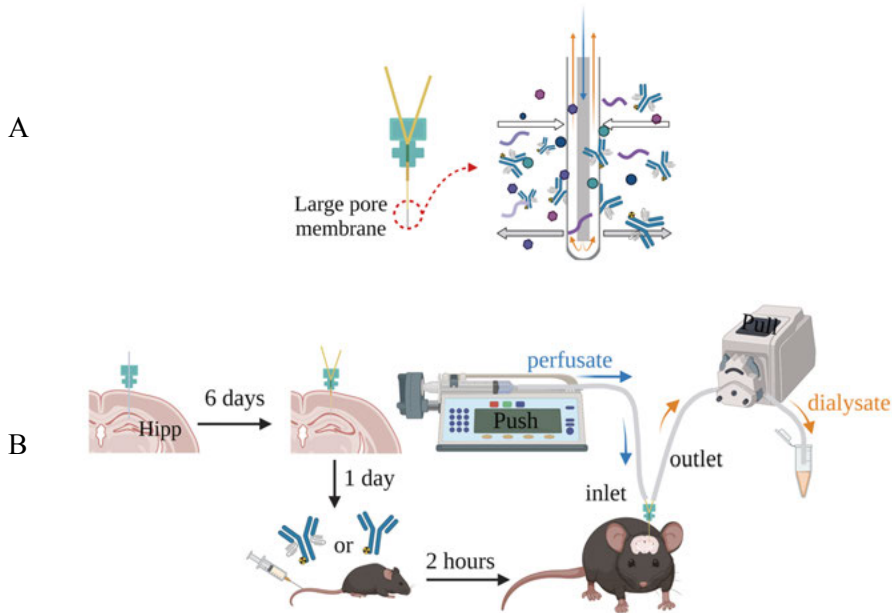


Fig. 8. Molecule exchange around the semi-permeable membrane of the microdialysis probe (A). Image adapted from Chaurasia et al. (2007)<sup>238</sup>. Flow chart of *in vivo* microdialysis (B). The setup of the surgical insertion of the microdialysis probe is similar to the surgery used for the deposition model shown in Fig. 4. The microdialysis guide cannula was inserted into the left hippocampus (Hipp) and secured on the skull.

In **Paper IV**, we tracked the ISF concentration of [<sup>125</sup>I]RmAb3D6 and [<sup>125</sup>I]RmAb3D6-ScFv8D3 by microdialysis. A guide probe was inserted into the hippocampus through stereotaxic surgery one week before the experiment. The guide was changed to a dialysis probe one day before the actual microdialysis experiment and the injection of the radiolabelled antibody. During the microdialysis, a push and pull system was used based on two synchronised pumps maintaining the perfusion flow. The dialysate was collected for later biochemical analysis (Fig. 8).

## Brain homogenisation

Brain homogenates are widely used in the preclinical evaluation of both endogenous and exogenous molecule concentrations in the brain. We mainly measured A $\beta$  and  $\alpha$ Syn levels in the studied mouse models. Measuring the concentration of different forms of A $\beta$  and  $\alpha$ Syn in the isolated brain can provide valuable information on disease progression and treatment effects.

In the thesis, brain homogenisation and protein extraction were used in all studies except in the study described in **Paper II**, which only included wild-type mice. Generally, we performed a serial extraction in tris-buffered saline

(TBS) or phosphate-buffered saline (PBS), TBS-triton (TBST), and formic acid (FA) using brain tissue from either selected regions or whole hemispheres (Fig. 9). The homogenisation was conducted by a bead-based automated homogeniser Precellys<sup>®</sup> Evolution (Bertin Technologies) and the process was adapted from published protocols<sup>205,239</sup>. The composition of proteins varies in different fractions. At least in theory, the TBS/PBS fraction contains soluble molecules, the TBST fraction contains the membrane-associated proteins, while the FA fraction represents the insoluble protein deposits.

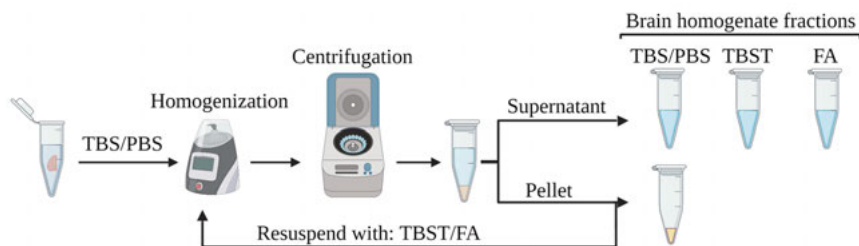


Fig. 9. Flow chart of brain homogenisation.

## Thin-layer chromatography (TLC)

TLC was used to check the radiometabolites in plasma and brain samples and also to investigate the stability of radiolabelled antibodies. In **Paper II**, metabolite analysis was done with brain homogenates to investigate if any radiometabolites were present in the brain. In **Paper III** and **IV**, TLC was used to examine if <sup>125</sup>I was attached to the antibodies in the plasma, brain and the brain ISF or if free <sup>125</sup>I was detected, which could be a sign of deiodination.

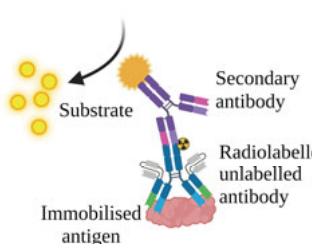
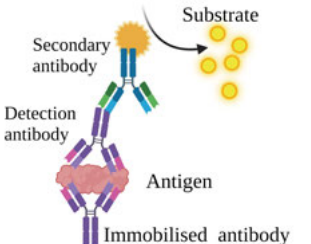
A drop of plasma, brain homogenate, or brain ISF dialysate was applied to a TLC plate and put in a solvent chamber. After the solvent was run for around 5 cm, the plate was dried and exposed to a phosphor imaging plate and scanned with a phosphor imager. When checking for deiodination, small molecules (e.g. free <sup>125</sup>I) move with the solvent, while larger molecules, such as antibodies, stay at the application spot. A reverse-phase aluminium TLC plate (silica gel) was used in the metabolite study for [<sup>18</sup>F]SynVesT-1. Here, polar compounds move with the soluble phase, while less polar compounds stay closer to the starting line.

## Enzyme-linked immunosorbent assay (ELISA)

ELISA is an immunoassay based on antibody-antigen interactions. It is a quantitative method for detecting and measuring antibody or antigen concentration in solution. Several types of ELISA exist for different purposes depending on the combination of antigens and antibodies. **Paper I-V** mainly

used indirect ELISA and sandwich ELISA. The combination of antibodies and the description of measurements are shown in Table 6. The secondary antibody is often conjugated with horseradish peroxidase (HRP). This enzyme can catalyse the oxidation of 3,3',5,5'-tetramethylbenzidine (TMB)-substrate, turning the chromogen from colourless into blue-green colour and generating a colourimetric signal with an intensity that is correlated to the amount of detection antibody. The redox reaction is stopped by acid application, and the complete TMB reaction leads to a yellow product with a significant absorbance at 450 nm<sup>240</sup>. The biotin-streptavidin conjugation system is often used in immunoassays, including ELISA. The two molecules bind to each other with high specificity and affinity, and biotin can often be added to biomolecules with simple and fast procedures.

Table 6. Set-up of ELISA in the thesis.

	<b>Indirect ELISA</b>	<b>Sandwich ELISA</b>
		
Immobilised antigen/antibody:	anti-mouse IgG mouse TfR A $\beta$ protofibril $\alpha$ Syn oligomer	anti-A $\beta$ 40 anti-A $\beta$ 42 mAb3D6 anti- $\alpha$ Syn antibody MJFR1
Detection antibody:	-	biotinylated-3D6 anti- $\alpha$ Syn antibody Clone 42
Secondary antibody:	HRP anti-mouse IgG F(ab') <sub>2</sub>	Streptavidin-HRP HRP anti-mouse IgG F(ab') <sub>2</sub>
Substrate:	TMB	TMB
Purpose:	To quantify the binding affinity of antibodies before and after radiolabelling	To quantify the concentration of proteins in brain homogenates.

HRP: horseradish peroxidase. TMB: 3,3',5,5'-tetramethylbenzidine.

## Staining

Immunohistochemistry staining is based on a similar principle of protein-protein interaction as in ELISA but relies on antibody binding to antigens on tissue sections. For chromogen staining, the secondary antibody was often conjugated with HRP, and fluorophore-labelled secondary antibodies were used

for immunofluorescence staining. Besides immunohistochemistry staining with antibodies, fluorescent dyes such as thioflavin-S (ThS) and thioflavin-T (ThT) can be directly applied on sections to visualise the fibrillar structure of amyloid<sup>241</sup>. All three types of stainings were used in the thesis, and the target of interest, antibody (for immunostaining) and dye (for simple staining) used in each paper are listed in Table 7. Chromogen staining was only used in **Paper III** to investigate  $\alpha$ Syn and A $\beta$  pathologies in post-mortem human brain sections. Subsequently, the signals were examined by a bright-field microscope (Nikon Eclipse 80i). Signals of all fluorescence staining were examined by a fluorescence microscope (Zeiss Observer Z.1).

Table 7. Target and ligand used in staining protocols

	<b>Target</b>	<b>Antibody used</b>	<b>Dye used</b>
Paper II	SV2A	anti-SV2A	
	Neuronal nuclear	anti-NeuN	
Paper III	$\alpha$ Syn	RmAb48, RmAbSynO2	
	APP	RmAb3D6	
	$\alpha$ Syn fibril	-	ThS
Paper IV	Astrocyte	anti-GFAP	
	Microglia	anti-Iba1	
Paper V	A $\beta$ 1-42	anti-A $\beta$ 42	
	amyloid plaques	-	ThS

NeuN: neuronal nuclear antigen. GFAP: glial fibrillary acidic protein. Iba1: ionised calcium-binding adaptor molecule.

## Funding

The thesis was performed at the Department of Public Health and Caring Sciences, Molecular Geriatrics, Rudbeck Laboratory, Uppsala University, Sweden. The work received financial support from the Swedish Research Council, Alzheimerfonden, Hjärnfonden, Torsten Söderbergs stiftelse, Åhlénstiftelsen, Magnus Bergvalls stiftelse, Stiftelsen för Gamla Tjänarinnor, Konung Gustaf V:s och Drottning Victorias Frimurarestiftelse, Stohnes stiftelse, Hedlunds stiftelse, VINNOVA, and Parkinsonfonden. This project also received funding from the European Union's Horizon 2020 research and innovation programme under the Marie Skłodowska-Curie grant agreement No 813528 (PET-AlphaSy).

Figure illustrations were created in BioRender.com.

# Aim

The overall aim of the thesis was to evaluate novel PET radioligands that can visualise diverse pathological changes in preclinical models of neurodegeneration. The specific aims were the following:

## **Paper I**

To characterise the binding of SV2A PET radioligand [ $^{11}\text{C}$ ]UCB-J in one AD (tg-ArcSwe) and one PD (L61) transgenic mouse model. Most importantly, to compare synaptic density in the transgenic models to age-matched wild-type control mice by using [ $^{11}\text{C}$ ]UCB-J PET.

## **Paper II**

To investigate if synaptic density decreases in ageing mice using the second-generation SV2A PET radioligand [ $^{18}\text{F}$ ]SynVesT-1. Moreover, to compare the pharmacokinetics of [ $^{18}\text{F}$ ]SynVesT-1 in three age groups of mice.

## **Paper III**

To use an antibody-based PET radioligand to image  $\alpha\text{Syn}$  brain pathology in mice with intracranial  $\alpha\text{Syn}$  deposits and PD mouse models.

## **Paper IV**

To explore and compare brain pharmacokinetics of  $\text{A}\beta$ -targeting monospecific antibody mAb3D6 and bispecific antibody mAb3D6-ScFv8D3 using microdialysis in a knock-in AD mouse model.

## **Paper V**

To investigate if anti- $\text{A}\beta$  treatment with antibody mAb158, i.e. the murine version of clinically investigated *Lecanemab*, inhibits the binding of amyloid PET radioligand [ $^{11}\text{C}$ ]PiB.

# Results and discussion

## Synaptic density change in neurodegenerative disease

Due to neurodegeneration, reduced synaptic density has been described in AD and PD patients, and this decrease has been visualised with [ $^{11}\text{C}$ ]UCB-J PET<sup>144,145,149</sup>. The synaptic loss has also been seen in some AD mouse models<sup>148</sup>, but it has not been studied in any PD mouse model previously<sup>147</sup>. Thus, we investigated synaptic density by [ $^{11}\text{C}$ ]UCB-J PET imaging in tg-ArcSwe and L61 mouse models and compared the PET signals to those obtained in non-transgenic wild-type age-matched controls, wt-ArcSwe and wt-L61. Retention of [ $^{11}\text{C}$ ]UCB-J in the mouse brain was first explored by model-free outcomes: AUC and AUC<sub>brain/blood</sub> ratio were calculated based on the TACs in the brain and the blood. In the studied brain regions, AUC in L61 and wt-L61 were generally higher than in the tg-ArcSwe and wt-ArcSwe mice.

Moreover, the transgenic mice displayed somewhat lower AUC than their respective wild-type control groups. However, no significant differences between transgenic and wild-type mice in AUC were found after *post hoc* correction in any studied regions, including blood. Taking radioactivity in the blood into account, the brain-to-blood partition coefficient, AUC<sub>brain/blood</sub> ratio, was calculated. Similar to AUC, AUC<sub>brain/blood</sub> ratio did not reveal a difference between tg-ArcSwe and wt-ArcSwe. However, the AUC<sub>brain/blood</sub> of L61 mice was around 12% lower than that observed in wt-L61 and was significantly decreased in the hippocampus ( $p = 0.04$ ).

Next, we explored the model-based outcome,  $V_T$ , to estimate brain retention of [ $^{11}\text{C}$ ]UCB-J. Overall, transgenic mice tended to have lower  $V_T$  than age-matched wild-type controls in all studied brain regions.  $V_T$  of tg-ArcSwe was approximately 5% lower than wt-ArcSwe, and  $V_T$  of L61 was around 12% less than observed in wt-L61. Despite an overall positive interactive effect of genotype on  $V_T$  in the L61 model (1TCM- $V_T$ ,  $F_{\text{genotype}}(1, 96) = 17.44$ ,  $p < 0.0001$ ), *post hoc* analysis did not reveal a difference between transgenic L61 mice and wild-type controls, wt-L61.

A previous study identified a 26% difference in hippocampus binding between APP/PS1 and wild-type mice<sup>148</sup>. The group differences between tg-ArcSwe and age-matched wild-type mice in our study were much smaller than the previously reported differences between wild-type and AD mice. This discrepancy is probably a consequence of the choice of the mouse model and analysis method. The APP/PS1 model exhibits more aggressive A $\beta$  pathology

caused by mutations in both the *APP* and the presenilin 1 (PS1) genes. Tg-ArcSwe, however, only harbours *APP* mutations. As for the method of analysis, Toyonaga et al. (2022) used a reference tissue-based kinetic model with the brain stem or the whole brain as the reference region, while our measurements were based on an input function. We also found that  $V_T$  generated by the three kinetic models correlated well with  $AUC_{\text{brain/blood}}$ , especially in L61 mice, indicating that  $AUC_{\text{brain/blood}}$  could be used as an alternative to full kinetic modelling in mice for simple and fast analysis.

Furthermore, we tried to correlate PET data with pathology. Levels of  $A\beta_{1-40}$ ,  $A\beta_{1-42}$ , and total  $\alpha\text{Syn}$  in the hippocampus, cortex and cerebellum of the PET-scanned mice were measured by ELISA. No direct correlation was found in any brain regions between the PET estimates and respective  $A\beta$  or  $\alpha\text{Syn}$  pathology. The measurements confirmed the existence of related pathology in the respective mouse models and the absence of pathology in the wild-type controls. The most abundant  $A\beta$  pathology was located in the cortex, while the cerebellum contained the lowest regional level of pathology. The variance in  $V_T$  between tg-ArcSwe and wt-ArcSwe matched the abundance of the pathology, e.g. the largest difference in  $V_T$  between tg-ArcSwe and wt-ArcSwe was in the cortex. In the L61 model, transmission electron microscopy results did not indicate a lower number of synapses in the L61 mouse compared to the wt-L61 mouse in the cortex, hippocampus and cerebellum, suggesting a resistant synaptic density during the progression of  $\alpha\text{Syn}$  pathology in this model.

We concluded that the synaptic density in tg-ArcSwe and L61 did not dramatically decrease compared to wild-type controls. Meanwhile, several group comparisons were close to becoming significant (e.g.  $AUC_{\text{thalamus/blood}}$ :  $p = 0.05$  for L61 versus wt-L61), and a large variation existed in ELISA. Thus, we believe that large groups of animals are needed to detect differences between models of neurodegeneration and wild-type mice with [ $^{11}\text{C}$ ]UCB-J. Furthermore, these potential differences are relatively subtle.

The study also suggested that age could affect synaptic density. The  $AUC_{\text{brain/blood}}$  ratio and  $V_T$  were reduced in the older wt-ArcSwe compared to younger wt-L61 mice. This result was not anticipated when designing the study, and the comparison was not completely accurate as the two groups of wild-type mice had slightly different genetic backgrounds to match their transgenic littermates (Table 1). Nevertheless, it was in line with some previously published results using wild-type mice of C657BL/6 genetic background<sup>148,196</sup>. Thus, in **Paper II**, the influence of age on synaptic density using wild-type mice from the same strain of wt-ArcSwe (C57BL/6) was investigated.

## Synaptic density in ageing

Based on the findings in **Paper I**, we continued to investigate synaptic density in ageing. The study included three age groups of C57BL/6 mice (3-4 months, 12-14 months, and 17-19 months), and a second-generation PET radioligand for SV2A imaging, [<sup>18</sup>F]SynVesT-1, was used instead of [<sup>11</sup>C]UCB-J. The two radioligands display similar pharmacokinetics, and the thalamus, striatum, and hippocampus displayed the highest brain retention. We also compared the 1TCM- $V_T$  for [<sup>11</sup>C]UCB-J (**Paper I**) and the 1TCM- $V_T$  for [<sup>18</sup>F]SynVesT-1 generated in **Paper II** in the same age group of mice (17-20 months) and found no difference between the two radioligands in any of the studied regions.

PET data analysis was similar to that in **Paper I**. Brain retention of [<sup>18</sup>F]SynVesT-1 was estimated by AUC of the TACs, and kinetic modelling was based on a heart IDIF. No difference in AUC was found between age groups. However, the  $V_T$  of [<sup>18</sup>F]SynVesT-1 exhibited a “bell-shape” relation with the highest  $V_T$  found in the middle-aged group. The 10 % difference of 1TCM- $V_T$  between the 3-4 months old mice and the 17-19 months old mice ( $p = 0.0284$ ) was smaller than the 12% difference between the 12-14 months and the 17-19 months mice ( $p = 0.0032$ ). Overall, synaptic density was slightly decreased in the 17-19 months old mice with no age-dependent difference at the regional-specific level. This is consistent with electron microscopy findings in humans that indicate a decline of synaptic density in the frontal cortex in subjects older than 74 years<sup>242</sup>. Also, human SV2A PET studies conducted in healthy subjects concluded that synaptic density is relatively stable during most of the lifespan. The apparent minor drop in synaptic density in subjects over 80 years old could result from brain atrophy, and this change was not significant after partial volume correction<sup>150,151</sup>. Although we could not examine possible brain atrophy with a detailed MRI, C57BL/6 mice may exhibit a similar loss in cortical brain region after the age of 17 months<sup>243</sup>, e.g. the oldest mice included in the study.

Later, we measured SV2A and the number of neurons using immunohistochemistry. Quantification of stainings was conducted in hippocampus CA1 and CA3 regions, constituting the information centre of the hippocampal and corticocortical circuits, passing information in several principal pathways<sup>244,245</sup>. Synaptic density in these regions is likely to be altered in cognitive-impaired ageing<sup>100</sup>. Nevertheless, consistent with the PET, SV2A was not altered between age groups, and the number of neurons also remained stable.

We believe the steady synaptic density measured in our study could have at least two explanations. One explanation is that SV2A lacks sensitivity as a target for capturing synaptic density changes in healthy ageing. SV2A is distributed abundantly in the whole brain, mainly in glutamatergic and GABAergic synapses, but the expression of excitatory and inhibitory synapses differs between brain areas<sup>246-248</sup>, and not all synapses are vulnerable to ageing<sup>93,249</sup>. Whether SV2A PET could capture the sophisticated but subtle synaptic

changes during healthy ageing remains to be studied. Two studies using independent component analysis for SV2A PET data, however, did conclude that age is associated with the intensity of the PET signals<sup>152,250</sup>.

The other explanation is that dramatic synaptic loss only happens in cognitive-impaired ageing but not in healthy ageing. Since cognitive impairment in ageing has enormous individual variation<sup>249</sup> and we did not include animals based on behaviour tests, nor did we conduct a longitudinal study using the same animals, our results could reflect a mixed group of both cognitive-impaired and healthy animals. Thus, the results should be interpreted with caution.

## Quantification of SV2A PET

We explored several different kinetic models for the quantification of SV2A PET in our mouse models. Without a true reference region in SV2A PET imaging, we concluded that reference tissue-based kinetic models, albeit used by others<sup>148,251</sup>, were not applicable. Instead,  $V_T$  was generated from 1TCM, 2TCM, and the Logan plot based on an IDIF acquired from the left ventricle of the heart<sup>195,196</sup>. All three models described the [<sup>11</sup>C]UCB-J data well without any further correction of the IDIF. Considering the goodness-of-fit parameters, the 1TCM proved more robust, as the 2TCM failed to converge for a few animals. Therefore, 1TCM was chosen to further characterise [<sup>11</sup>C]UCB-J PET in mice. This was consistent with published results from humans and rodents<sup>137,196,252</sup>. However, it should be noted that using  $V_T$  derived from 2TCM or the Logan plot would not have changed the conclusion regarding differences in synaptic density between pathology models and wild-type controls. For [<sup>18</sup>F]SynVesT-1, metabolite and plasma-to-whole blood corrections were needed<sup>253</sup>. As expected, based on these previous studies and human data<sup>140</sup>, 2TCM with a metabolite-corrected IDIF described the data best, although also 1TCM performed well.

The acquisition time of the [<sup>11</sup>C]UCB-J scan was 60 min. The kinetics of [<sup>18</sup>F]SynVesT-1 was somewhat slower than for [<sup>11</sup>C]UCB-J, and the published results in wild-type and APP/PS1 mice by the time we started our study suggested that a 90-min acquisition was preferable<sup>251</sup>. To evaluate if the acquisition time of [<sup>18</sup>F]SynVesT-1 could be shortened, we correlated  $V_T$  estimated from 90-min PET data to the estimates from 60-min data in all studied brain regions. In all kinetic models,  $V_T$  estimated from 90 min and 60 min PET data were in excellent agreement in all brain regions ( $p < 0.0001$ ). Good correlations were also shown for  $K_1$  ( $p < 0.0001$ ). Based on the ratio of  $V_{T, 60\text{min}}$  and  $V_{T, 90\text{min}}$  ( $V_{T, 60\text{min}} / V_{T, 90\text{min}}$ ), we observed that compartmental models overestimated  $V_T$  by around 9%, while the Logan plot overestimated  $V_T$  by 13% when 60-min data was used. Thus, we concluded that a 60-min acquisition time was enough to quantify [<sup>18</sup>F]SynVesT-1 binding in mice if a compartmental model

was used for analysis. The shortening of the scanning time is consistent with the findings of  $V_T$  time stability between 120 and 60 min, as reported in a recent study<sup>253</sup>.

## Visualising $\alpha$ Syn with antibody-PET

Aggregates of  $\alpha$ Syn are one of the hallmarks of PD besides synaptic dysfunction. The distribution and transmission of  $\alpha$ Syn aggregates in different brain regions are of great interest for understanding the disease progression in PD and other synucleinopathies. Bispecific antibodies engineered to cross the BBB via TfR have proven to be a promising strategy for antibody modulation of intrabrain targets. Moreover, A $\beta$  pathology in transgenic AD mice can be imaged through PET using radiolabelled bispecific RmAb158-scFv8D3<sup>178,179,254,255</sup>. We then focused on developing new radioligands for imaging  $\alpha$ Syn based on bispecific antibodies. Five antibodies with slightly different binding profiles towards  $\alpha$ Syn and mouse TfR were generated (Table 2). All antibodies display high affinities for larger  $\alpha$ Syn oligomers and protofibrils.

We first characterised the *in vitro* properties of the <sup>125</sup>I- and <sup>124</sup>I-labelled antibodies. After radiolabelling, affinities of the bispecific antibodies towards mouse TfR were slightly reduced but the affinities towards  $\alpha$ Syn remained constant (**Paper III**, Fig. 2). Autoradiography with <sup>125</sup>I-labelled antibodies showed that the binding of the bispecific antibodies to brain sections prepared from L61 mice was generally higher than the binding observed for unmodified antibodies. This became more evident after blocking sections with unlabelled antibodies (self block) or 8D3 (mouse-TfR block), suggesting that the positive signals were mainly derived from antibody binding to  $\alpha$ Syn. Two bispecific antibodies, RmAb48-scFv8D3 and RmAbSynO2-scFv8D3, with the highest selectivity for  $\alpha$ Syn aggregates over monomers, were tested on human post-mortem tissue sections. Sections from PD, AD, and MSA patients and a non-demented elderly control were used. The bispecific antibodies showed specific binding to putamen sections from MSA patients and substantia nigra sections from PD patients. Furthermore, the antibodies did not specifically bind to AD and control brain sections, indicating their high selectivity towards  $\alpha$ Syn over A $\beta$ . This discrimination between  $\alpha$ Syn and A $\beta$  is especially desirable as the development of PET radioligands targeting  $\alpha$ Syn based on small molecules has been hampered by cross-reactivity towards A $\beta$ .

For *in vivo* characterisation, an initial biodistribution study was performed in wild-type mice. Brain retention of the <sup>125</sup>I-labelled bispecific antibodies in mice 2 h post-injection was 26- to 63-fold higher than the brain retention observed with their unmodified IgG formats. Next, [<sup>124</sup>I]RmAbSynO2-scFv8D3 was evaluated in the  $\alpha$ Syn deposition model in which the intracranially deposited  $\alpha$ Syn fibrils were visualised as a high-intensity spot, while no signal was

detected with [ $^{124}$ I]RmAbSynO2 (**Paper III**, Fig. 6). In addition, no signal was derived from the PBS injected brain with either radioligand. Further, the two most promising bispecific antibody-based ligands, [ $^{124}$ I]RmAb48-scFv8D3 and [ $^{124}$ I]RmAbSynO2-scFv8D3, were injected into L61, A30P mice and wild-type controls. Mice were PET scanned for 60 min at 72 h post ligand injection. Despite high brain uptake and specific binding to  $\alpha$ Syn *in vivo* in the deposition model, the two ligands displayed low brain uptake in all brain regions and could not detect human  $\alpha$ Syn expressed in the transgenic mice. In addition, no difference was observed between L61 and A30P compared to wild-type controls. The reason for this could be the intracellular location of  $\alpha$ Syn. PET ligands must likely also pass the cell membrane after crossing the BBB to interact with the intracellular  $\alpha$ Syn. It has been shown that neurons express TfR, and TfR-binders are found inside neurons<sup>256,257</sup>. Thus, in theory, intracellular targets can be reached. However, the amount of ligand available for transport into the cell will depend on the unbound ligand concentration in ISF (Fig. 10). In this experiment, we did not determine the concentration of [ $^{124}$ I]RmAb48-scFv8D3 and [ $^{124}$ I]RmAbSynO2-scFv8D3 in the ISF. Thus, the question regarding the free fraction of bispecific antibodies in ISF remained.

## Understanding the pharmacokinetics of bispecific antibodies

To further understand the kinetics of bispecific antibodies in the brain, in particular in the ISF, we studied and compared brain pharmacokinetics of A $\beta$ -targeting bispecific antibody RmAb3D6-scFv8D3 and unmodified monospecific antibody RmAb3D6 using microdialysis in **Paper IV** (Fig. 10).

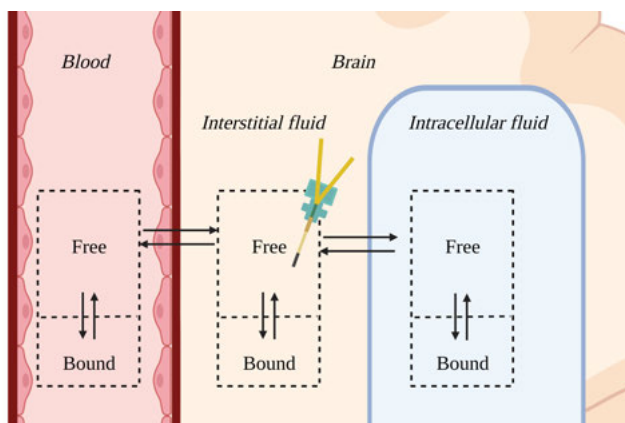


Fig. 10. Microdialysis measures the unbound drug in interstitial fluid (ISF).

Antibody RmAb3D6 is the murine version of the clinically studied antibody *Bapineuzumab*. Microdialysis was performed after intravenously injecting *App*<sup>NL-G-F</sup> and wild-type C57BL/6 control mice with <sup>125</sup>I-labelled antibodies. Dialysates representing ISF in the hippocampus were collected and analysed. The concentration of [<sup>125</sup>I]RmAb3D6-scFv8D3 in the ISF increased throughout the measurement, while [<sup>125</sup>I]RmAb3D6 reached a plateau after approximately 5 h. At 6 h post-injection, [<sup>125</sup>I]RmAb3D6-scFv8D3 concentration was 2-fold higher than the [<sup>125</sup>I]RmAb3D6 concentration in the ISF. Meanwhile, the total brain concentrations differed 8-fold, indicating that a large portion of the [<sup>125</sup>I]RmAb3D6-scFv8D3 remained associated with the brain, potentially bound to some extent to the capillaries<sup>186</sup>. At 24 h post-injection, brain concentration of [<sup>125</sup>I]RmAb3D6-scFv8D3 in wild-type mice fell sharply to the same level as [<sup>125</sup>I]RmAb3D6. However, in *App*<sup>NL-G-F</sup> mice, the [<sup>125</sup>I]RmAb3D6-scFv8D3 concentration was still significantly higher than that observed for [<sup>125</sup>I]RmAb3D6 ( $p = 0.024$ ). In both *App*<sup>NL-G-F</sup> and wild-type mice, the ISF-to-plasma ratio of [<sup>125</sup>I]RmAb3D6-scFv8D3 was higher than that of [<sup>125</sup>I]RmAb3D6 (wild-type:  $p = 0.0062$ ; *App*<sup>NL-G-F</sup>,  $p = 0.0003$ ), suggesting that [<sup>125</sup>I]RmAb3D6-scFv8D3 enters the brain parenchyma and that the total brain concentrations are not based on antibody residing in the endothelial cells of the BBB.

*Ex vivo* autoradiography after microdialysis indicated that the distribution of [<sup>125</sup>I]RmAb3D6-scFv8D3 was uniform, while [<sup>125</sup>I]RmAb3D6 accumulated around the probe insertion area, similar to the control mice which were injected with a high concentration of sodium [<sup>125</sup>I]iodide. Further, immunohistochemistry staining of Iba1 and GFAP suggested an elevated inflammation level around the probe area, indicating that the insertion of the cannula had triggered an immune response. This has not been discussed in previous microdialysis studies with antibodies<sup>235,258,259</sup>. The compromised BBB and the activated immune response could lead to inaccuracies in the antibody concentration measurements in the ISF and is more critical for regular monospecific antibodies with low delivery across the BBB.

The study confirmed that the bispecific antibody had a distinct kinetic profile, crossed the BBB, and reached the ISF better than the monospecific antibody. In addition, this is the first microdialysis study aiming to understand the brain pharmacokinetics of bispecific antibodies targeting TfR and A $\beta$ . Despite the challenges, microdialysis remains a unique method to follow the brain pharmacokinetics of radiolabelled antibodies in real time.

## Antibody treatment effect on PET imaging

Most clinical studies of therapeutic anti-A $\beta$  antibodies have used amyloid PET to include subjects in the trials and to assess drug effects<sup>74,260</sup>. The PET results in recent clinical trials of anti-A $\beta$  antibodies *Aducanumab*<sup>74</sup> and

*Lecanemab*<sup>73,260</sup> initiated the study in **Paper V**. Successful elimination of A $\beta$  plaques after 12-18 months of treatment was indicated by a substantially decreased amyloid PET signal in patients. In many cases, patients even became “amyloid-negative” and were thus comparable to healthy controls. However, this decrease in brain amyloid as measured by amyloid PET has not been matched by a similar substantial effect on cognitive function and brain A $\beta$  pathology reduction after treatment has so far not been investigated by extensive *post mortem* analyses of brain tissue isolated from AD patients<sup>261</sup>. Thus, we investigated if amyloid PET signals are altered after a short-term anti-A $\beta$  antibody treatment and if the potential alteration is caused by clearance of A $\beta$  or partly by blocking the binding sites of the amyloid PET radioligands.

In the study, *in vitro* ThS staining was first performed on brain sections prepared from tg-ArcSwe mice and pre-incubated with RmAb158 or PBS. Next, age-matched tg-ArcSwe mice were treated with RmAb158 or PBS for three weeks before being i.v. administered with [<sup>11</sup>C]PiB and euthanized at 40 min post-injection. The isolated brain was extracted and divided into two hemispheres. *Ex vivo* autoradiography was performed using one hemisphere, and radioactivity in the other hemisphere was measured by gamma-counter for SUV calculation and subsequently homogenised for total A $\beta$ 40 and A $\beta$ 42 detection.

The integrated density of *in vitro* ThS staining in the frontal cortex was similar on brain sections pre-incubated with RmAb158 and PBS. Next, brain tissue sections prepared from animals treated with either RmAb158 or PBS prior to [<sup>11</sup>C]PiB administration were studied in *ex vivo* autoradiography. Although RmAb158-treated animals tended to display a lower [<sup>11</sup>C]PiB binding than PBS-treated animals, no group differences were found. Consistent with this, SUV in the cerebrum and cerebellum was similar in the two treatment groups. A $\beta$  pathology measured by ELISA in brain homogenates indicated that the two treatment groups had comparable amounts of A $\beta$ <sub>1-40</sub> and A $\beta$ <sub>1-42</sub> in the brain. This suggested that the short-term treatment did not reduce the amount of A $\beta$  plaques that can be visualised by [<sup>11</sup>C]PiB. This was anticipated as the study was designed to enable investigation of RmAb158’s ability to block [<sup>11</sup>C]PiB binding rather than its influence on the actual pathology. Moreover, [<sup>11</sup>C]PiB binding correlated with A $\beta$ 40 brain levels, i.e. the dominant pathology in the tg-ArcSwe brain, and thus, demonstrated that [<sup>11</sup>C]PiB binding reflects A $\beta$  pathology in the tg-ArcSwe brain. The study supported the notion that reduced the amyloid PET signal in clinical trials is mainly due to the elimination of amyloid.

## Conclusion and future perspectives

From [ $^{18}\text{F}$ ]FDG to [ $^{11}\text{C}$ ]PiB, and from small molecules to antibody-based ligands, PET imaging in neurodegenerative diseases has not had a very long history but is a fast-developing field. With a better understanding and deepened knowledge of the diseases and associated pathology progression, new ligands for visualising different pathological features of neurodegenerative diseases are emerging every year. Sometimes with joy, sometimes with distress. Still, we manage to obtain valuable information on the way.

In the initial studies, we optimised a modelling method based on IDIF in tg-ArcSwe and L61 transgenic mouse models, which can be used to characterise new ligands in the future. Our data suggested that [ $^{11}\text{C}$ ]UCB-J PET can display decreased synaptic density in tg-ArcSwe and L61 mouse models but only in the regions with the most abundant pathology. Moreover, the cross-sectional study using [ $^{18}\text{F}$ ]SynVesT-1 proposed that synaptic density was somewhat decreased in the oldest group, but the overall synaptic density was rather unchanged with potentially some fluctuations, indicating the highest synaptic density in the middle-aged group. Admittedly, conducting a longitudinal study using the same animals and measuring the synaptic density change along ageing would be more beneficial. Still, the two studies indicated that C57BL/6 is a suitable and stable mouse model for studying ageing synapses. The studies also established quantification methodology for SV2A PET in translational imaging.

Traditional PET radioligands are small molecules. With proper characteristics such as high lipophilicity, small molecules can cross the BBB, but lack of specificity and selectivity may cause a high background signal. This remains an unconquered challenge for PET ligands in PD and AD imaging, especially for developing radioligands for  $\alpha\text{Syn}$ . In this thesis, bispecific antibodies are proposed as an alternative solution. To prove this concept, we developed antibody-based PET ligands targeting  $\alpha\text{Syn}$  aggregates with high specificity and selectivity, and tested the approach for *in vivo* imaging of  $\alpha\text{Syn}$ . Using this strategy, we could target extracellular deposits of  $\alpha\text{Syn}$ , but not endogenously expressed intracellular  $\alpha\text{Syn}$ . We, therefore, conclude that for successful  $\alpha\text{Syn}$  imaging, a ligand must enter the cytoplasm after crossing the BBB to reach the intracellular  $\alpha\text{Syn}$  aggregates. A new antibody design or a new transporter system may thus be needed.

Microdialysis is an advanced but somewhat complicated and time-consuming procedure. However, it provides unique information about free drug concentrations compared to the total concentrations measured by PET imaging. The study conducted within the project enhanced our understanding of the brain pharmacokinetics of bispecific antibodies targeting TfR and A $\beta$ . However, the long biological half-lives of antibodies would ideally require longer study times than the 24 h used in the present study. It would be interesting to track the entire kinetic profile of a regular antibody and compare it to the bispecific antibody to fully understand the potential benefits of bispecific brain-penetration antibody formats. Moreover, comparing the kinetics of RmAb3D6 and RmAb158, i.e. two different A $\beta$  antibodies, would also be enlightening. It may provide new information for the future design of anti-A $\beta$  antibodies.

The development of amyloid PET radioligands stimulates the advancement of diagnostic imaging techniques and provides benefits for clinical trials of anti-A $\beta$  immunotherapies for AD. Through the [ $^{11}\text{C}$ ]PiB study in RmAb158 treated mice, we hope to contribute to an increased understanding of how amyloid PET results should be interpreted when antibody intervention is present and to assist in the design of effective A $\beta$ -specific PET radioligands.

# Popular science summary

The elderly population in many countries is growing remarkably fast, and we are entering an ageing society. Dementia is not a part of healthy ageing. It is a syndrome of brain diseases with impaired cognitive function that affects daily life. Currently, around 50 million people worldwide have dementia, which is expected to triple by 2050, making it a global public health priority<sup>262</sup>.

Dementia is commonly seen in patients with neurodegenerative diseases. Alzheimer's diseases (AD) and Parkinson's disease (PD) are the two most common neurodegenerative diseases. During disease progression, the brain's functional information unit, the synapse, is gradually compromised and eventually degenerates, accompanied by neuronal death. Since synaptic loss strongly correlates with cognitive decline, imaging brain synapses provides an approach for mapping functionally impaired synapses in AD and PD. Positron emission tomography (PET) is a molecular imaging technique that can visualise various targets in the brain. A PET scan is an imaging test based on injecting a trace amount of radiolabelled molecules (radioligand) in the living subject (normally through the vein) and detecting the abnormal distribution of the radioligand in diseased conditions. It is widely used to assist in the diagnosis of cancer, heart diseases, and brain disorders. However, current PET radioligands are not ideal for diagnosing AD and PD. Therefore, developing suitable PET radioligands for the early and accurate detection of the two diseases is of great interest.

In **Paper I**, a PET radioligand targeting a synaptic protein, SV2A, was used to look for synaptic loss in AD and PD mouse models. Because SV2A is a membrane protein expressed on most of the synaptic vesicles, imaging of SV2A can estimate the density and location of functional synapses. SV2A PET revealed that synaptic loss only occurred in PD mice in the hippocampus, a brain region with an important role in learning and memory. It also suggested that the largest difference between mice with AD pathology and age-matched healthy controls was in regions with the most abundant pathology, such as the cortex. However, the pathology did not correlate with the SV2A PET signals, suggesting that several mechanisms are involved in cognitive impairment. These findings are consistent with PET results obtained in humans, which indicate that synaptic loss is not present in the whole brain but only located in specific regions such as the cortex and hippocampus.

Moreover, we used SV2A PET in three age groups of healthy mice and studied synaptic alteration during ageing. Interestingly, synaptic density did not gradually decrease with age. The middle-aged group had the highest synaptic density overall, followed by the young and the old age groups. This difference was based on a whole brain level. However, when looking at specific brain regions, e.g. the hippocampus, no difference in synaptic density was found between the age groups. The relatively stable synaptic density indicates that the synapse is fairly resistant to ageing. Together with other evidence in **Paper II**, it is concluded that synaptic dysfunction rather than density is more critical in cognitively impaired ageing.

Several pathological proteins are responsible for neurodegenerative diseases. Amyloid-beta ( $A\beta$ ) aggregates are believed to be one of the leading causes of AD. In comparison, alpha-synuclein ( $\alpha$ Syn) aggregates are responsible for PD. The natural form of  $A\beta$  and  $\alpha$ Syn exist in the healthy human body. Under diseased conditions,  $A\beta$  and  $\alpha$ Syn misfold and aggregate, turning into soluble assemblies (oligomers and protofibrils) and eventually insoluble plaques (fibrils). Different pools of  $A\beta$  and  $\alpha$ Syn aggregates have unique features and can cause distinct body damage. Recent studies aim to develop a PET radioligand targeting the most toxic pool of  $A\beta$  and  $\alpha$ Syn aggregates: protofibrils.

One of the challenges in developing such a radioligand is specificity, meaning that the radioligand should only bind to its target. The other challenge is that the ligand must cross the blood-brain barrier (BBB) and reach the target in the brain. Traditional PET radioligands based on small molecules can cross the BBB but sometimes lack specificity, as they tend to bind to other structures in addition to the primary target. Antibody-based radioligands are highly specific but can barely cross BBB. Taking advantage of existing brain transport systems, we designed the antibody in a *bispecific* format and used a strategy named after the Trojan horse to carry the antibody into BBB. On the blood side, the bispecific antibody binds to the transferrin receptor, TfR (the “horse”), which is highly expressed in regular blood vessels and typically carries iron into the brain. Here, the TfR will carry the bispecific antibody across the BBB to the brain, where it is released from the TfR and can bind to its primary target. In **Paper III**, we tested five bispecific antibodies with high specificity towards  $\alpha$ Syn protofibrils as potential PET radioligands. The promising candidate successfully imaged deposited  $\alpha$ Syn in the brain but failed to visualise endogenously expressed human  $\alpha$ Syn in PD mouse models. We speculate that this is due to the intracellular localization of most of the  $\alpha$ Syn pathology in the mouse models, making it unavailable to the bispecific antibody.

In order to gain more insight into the properties of bispecific antibodies entering the brain, we conducted a microdialysis study to discover the percentage of injected antibodies that can truly reach the target. We compared the

brain concentration profile of the bispecific antibody and its unmodified monospecific format, i.e. we investigated brain absorption, distribution, and elimination in **Paper IV**. We concluded that the bispecific antibody has a distinct brain concentration profile that differs from the unmodified antibody. Net absorption of the bispecific antibody continued during 6 h of measurement but was almost zero for the unmodified antibody after 5 h. A larger portion of the bispecific antibody entered the brain from blood and was distributed to the whole brain, while the unmodified antibody circulated in the blood and had limited distribution in the brain. After 24 h, there was still a substantial amount of bispecific antibody left in the brain, but hardly any unmodified antibody. The study indicated that bispecific antibodies better cross the BBB and could thus constitute a class of improved pharmaceuticals for brain disorders.

Despite its many advantages, microdialysis is an invasive method that requires the insertion of an experimental probe into the brain. In the study, we raise the caution of inflammation caused by the microdialysis probe insertion, potentially leading to the accumulation of antibodies around the probe region due to the possible damage caused to the brain tissue. This can lead to inaccuracy in the estimation of antibody concentration measurement.

Despite limited BBB penetration, two antibodies targeting A $\beta$  have shown positive treatment effects and have recently been conditionally approved as AD treatments in the US. Same for other clinical trials of anti-A $\beta$  therapies, two major assessments of treatment effect were amyloid PET and cognitive tests. Based on amyloid PET, the signals decreased significantly and even became negative after the treatment, indicating that anti-A $\beta$  therapies reduce A $\beta$  plaque load. However, this did not match with the continuous drop in cognitive abilities of the patients. It raises the concern that the anti-A $\beta$  antibodies somehow block PET signals without thoroughly clearing A $\beta$ , causing an overestimation of the A $\beta$  removal. In **Paper V**, we tested this hypothesis in an AD mouse model. The study indicated that amyloid PET imaging represents major A $\beta$  pathology in the brain. The reduction of PET signals in clinical trials was caused by the removal of A $\beta$  plaques.

In the thesis, we tested various PET radioligands to visualise different aspects of physiology and pathology in AD, PD and ageing. We aim to find PET radioligands that can contribute to an increased understanding of underlying biological processes in these conditions and enable differentiation between healthy and diseased conditions. We believe that our studies help to enhance the knowledge of how results obtained with these PET radioligands should be interpreted and aid in developing novel PET ligands for AD and PD.

# Acknowledgements

The seasons rotate, and time flies. Now it is another spring that is cold and white. Although the weather in Uppsala is not very friendly, the kind and skilful people here brighten my life. Your passion for science and life has supported me during this PhD journey and will benefit me in the future.

First and foremost, I am grateful for my supervisor team. You encourage and inspire me greatly, especially my main supervisor **Stina Syvänen**. Running a project is like joining a huge maze. Once we step in, many details are attractive and disorienting. I often lost myself in the side tracks, and you always guided me back to the main way but also encouraged me to follow my thoughts and explore the hidden corners. In addition, your keen insight can point out my feelings even before I am aware of them. It is tremendous, and I sincerely appreciate it. Second, my co-supervisor **Sahar Roshanbin**. Your enthusiasm can always release the pressure and light the way. Talking to you is so pleasant that somehow you became the only listener of my weird science knowledge during our experiments. I hope that was not too disturbing. Next, my second co-supervisor **Joakim Bergström**. Listening to your experience of the lovely but complicated synaptic proteins with the unique Japanese touch is very interesting. I miss the days when you were in the lab.

**Dag**, as I accidentally said in one of the consortium meetings, you are my unsung supervisor. All those days with ELISA and homogenisation, thanks for saving me from the crushed glass, broken machine, and lousy results.

Gratitude to the radiochemistry group and my chemistry mentors: **Jonas** and **Johanna**. Your dedication makes my sweaty running in the basement tunnel very worthwhile! And thanks for the exam-free radiochemistry tutorials.

For the MolGers, **Martin**, the experience with you in the memory clinic is unforgettable. It is striking but also inspiring when textbook information turns into living cases. **Anna**, thanks for the synapse knowledge and tips. Besides science, I learned a lot about Swedish culture from you. I hope your boat can win the family competition this year! **Ximena**, without your work behind the scenes, no experiment plan can run smoothly. Big thanks! It is also very nice talking with you about Japan and Korea, which makes me feel closer to home.

**Vilmantas**, thanks for finding solutions whenever I had an IT-related panic, and congrats on finding new mutations related to AD! **Agnesizka**, thanks for being a great work, swimming, and fika partner. You encourage me in so many ways. As promised, the two boxes of Ferrero Rocher are still in my drawer. Mentioning swimming, my other Fitbit friend, **Ulrika**, cheers for the microdialysis summer, and thanks for motivating me to exercise and eat healthily.

For the graduated students in MolGer, you all helped considerably. **Jinar**, I have admired your ability to explain results and answer questions with ease and fluency, just like Rebecca. Your nods from the audience boost my confidence when presenting. The two big brothers in the PET group: **Silvio**, thank you for the staining protocols and spaghetti recipe. Good luck finding a desirable job! **Tobbe G**, thank you for teaching and helping me with many experimental attempts. Whether it is microscope settings or müsli selection, you can always give a clue. **Maria**, my appreciation for taking care of me when I was injured. Together with **Evangelos**, thanks for being great office mates and helping me start my doctoral life. **Anish**, fun lunch chat partner. You are indeed a great information source. **Emma**, thanks for the cinnamon bun tutorial and all the kindness. Talking to you cheers me up. And **Rebecca**, I moved the sentences here from the following paragraph in the last review. Congrats! Thanks for all the help in science and daily life. Your hour-long project meetings impress me very often, and I hope to be as efficient as you. **Tsong**, although we did not physically work together, talking to you helps my experiment, writing and future decisions.

For the current students, **Eva**, although you do not identify yourself as a chemist, I still want to thank you for your help with the synthesis. Also, thanks for all the intriguing videos and apps you shared. **Gillian**, my “go-to” person for almost everything. Thanks again for the editing. You are a fantastic colleague and friend. Words cannot describe how great you are! I treasure all the memories we spent together in work and life. **Chiara**, thanks for the mitochondria talk. I named the day “mitochondria day” after our meeting. It is held once per year. **Tobias M**, I am glad to be introduced to your tau öl. It may have special effects when combined with sauna baths (Laukkanen et al., 2017. Age and ageing). **Amelia**, I believe you are talented in writing and game organising. Good luck with your inflammation PET adventure! **Abdul**, you are a nice and easy person to talk to. As the youngest, officially registered doctoral student in our lab (just a few days later than Amelia), I wish you all the best. **Elin**, thanks for the joint effort in microdialysis and tracer injection. I wish you all the best for a PhD life. For new members. **Wojciech**, congratulations on the grants and good luck with your future with organelles! **Sara Lopes**, the only person who has experienced the same previous and current bosses as me, I hope you also enjoy life in Uppsala. Thanks for the good coffee and office time for **Tiffany**, **Khalid**, and **Elnaz**!

And thanks for all the discussions about the statistics from the former MolGer members **Linn, Agata, and Sara**. I was forced to think more independently once all of you left the lab.

I also appreciate the good collaborations with **Greta Hultqvist, Linda Söderberg**, and PET-AlphaSy members.

Thank you to everyone in the PET-AlphaSy consortium, from project leader **Matthias Herth** to manager **Ulla Kløve Jakobsen**. Special thanks to the supervisors and students in BioArctic, University of Copenhagen and NRU, Rigshospitalet. Thanks to **Johanna Fälting, Olof Zachrisson, Ken Honek, Ronny Falk** and **Patrik Nygren** at BioArctic, who welcomed and guided me to an industrial research environment. Great appreciation to **Hanne Deman Hansen, Gitte Moos Knudsen, Nakul Raval, and Clara Madsen** for your enormous help during my time in Copenhagen and efforts to interpret the results. It is nice to go back to NRU, and I am jealous of the fabulous view from the new lab. I would also like to thank **Vladimir Shalgunov** and **Mikael Palmer** for your continued help with methodologies. Thank you, **Ran Sing**, for being a precious friend. The days working and baking with you in Uppsala were memorable. I hope your thesis writing is going well.

I would also like to mention **Sergio, Veronika, Ola, Ram** and **Pierre** at the Preclinical PET-MRI platform. Thank you for solving all the instrument and animal obstacles. My work would not have gone as far without your help. Many thanks to **Karin Staxäng** and **Monika Hodik** at Biovis TEM facility. TEM is a fun experience.

To my friends **Tianqi** and **Yongsheng**, thanks for sharing good food and life tips. **Kehuan, White, Honglian** and **Kim**, thanks for the travelling companions and hotpot memories, and for making my life more colourful.

踽踽独行，已是六七个春秋。感谢父母当年支持我出国读研，由此进入一个个不曾领略过的世界。时光如掷，记得当时你们还担心我无法完成学业，转眼博士答辩已经近在眼前。长路漫漫，不敢盼鹏北海，凤朝阳，但愿能长虑顾后，长乐未央。

# References

1. Phelps, M. E. *et al.* Tomographic measurement of local cerebral glucose metabolic rate in humans with (F-18)2-fluoro-2-deoxy-D-glucose: Validation of method. *Ann. Neurol.* **6**, 371–388 (1979).
2. GBD 2016 Dementia Collaborators. Global, regional, and national burden of Alzheimer’s disease and other dementias, 1990–2016: a systematic analysis for the Global Burden of Disease Study 2016. *Lancet Neurol.* **18**, 88–106 (2019).
3. GBD 2016 Parkinson’s Disease Collaborators. Global, regional, and national burden of Parkinson’s disease, 1990–2016: a systematic analysis for the Global Burden of Disease Study 2016. *Lancet Neurol.* **17**, 939–953 (2018).
4. Parkinson, J. An essay on the shaking palsy. *J. Neuropsychiatry Clin. Neurosci.* **14**, 223–236 (2002).
5. Trétiakoff, C. Contribution a l’étude de l’Anatomie pathologique du Locus Niger de Soemmering avec quelques deduction relatives a la pathogenie des troubles du tonus musculaire et de la maladie de Parkinson. *Theses de Paris* (University of Paris, 1919).
6. Lewy, F. H. & Lewandowsky, M. *Handbuch der Neurologie.* Berlin Jul. Springer (1912).
7. Spillantini, G. M. *et al.* alpha-Synuclein in Lewy bodies. *Nature* **388**, 839–840 (1997).
8. Polymeropoulos, M. H. *et al.* Mutation in the alpha-synuclein gene identified in families with Parkinson’s disease. *Science* **276**, 2045–2047 (1997).
9. Spillantini, M. G., Crowther, R. A., Jakes, R., Hasegawa, M. & Goedert, M.  $\alpha$ -Synuclein in filamentous inclusions of Lewy bodies from Parkinson’s disease and dementia with Lewy bodies. *Proc. Natl. Acad. Sci. U. S. A.* **95**, 6469–6473 (1998).
10. Grazia Spillantini, M. *et al.* Filamentous  $\alpha$ -synuclein inclusions link multiple system atrophy with Parkinson’s disease and dementia with Lewy bodies. *Neurosci. Lett.* **251**, 205–208 (1998).
11. Chahine, L. M. *et al.* In vivo distribution of  $\alpha$ -synuclein in multiple tissues and biofluids in Parkinson disease. *Neurology* **95**, E1267–E1284 (2020).
12. Donadio, V. *et al.* Skin  $\alpha$ -synuclein deposits differ in clinical variants of synucleinopathy: an in vivo study. *Sci. Rep.* **8**, 1–10 (2018).
13. Postuma, R. B. *et al.* MDS clinical diagnostic criteria for Parkinson’s disease. *Mov. Disord.* **30**, 1591–1601 (2015).
14. Jankovic, J. Parkinson’s disease: Clinical features and diagnosis. *J. Neurol. Neurosurg. Psychiatry* **79**, 368–376 (2008).
15. Chaudhuri, K. R., Healy, D. G. & Schapira, A. H. V. Non-motor symptoms

- of Parkinson's disease: diagnosis and management. *lancet Neurol.* **5**, 235–245 (2006).
16. Balestrino, R. & Schapira, A. H. V. Parkinson disease. *Eur. J. Neurol.* **27**, 27–42 (2020).
  17. Pihlström, L. & Toft, M. Genetic variability in SNCA and Parkinson's disease. *Neurogenetics* **12**, 283–293 (2011).
  18. Chartier-Harlin, M.-C. *et al.*  $\alpha$ -synuclein locus duplication as a cause of familial Parkinson's disease. *Lancet* **364**, 1167–1169 (2004).
  19. Singleton, A. B. *et al.*  $\alpha$ -Synuclein Locus Triplication Causes Parkinson's Disease. *Science* **302**, 841 (2003).
  20. Zappia, M. *et al.* Sex differences in clinical and genetic determinants of levodopa peak-dose dyskinesias in Parkinson disease: An exploratory study. *Arch. Neurol.* **62**, 601–605 (2005).
  21. Leentjens, A. F. *et al.* Modeling depression in Parkinson disease. *Neurology* **81**, 1036–1043 (2013).
  22. Cotzias, G. C., Van Woert, M. H. & Schiffer, L. M. Aromatic Amino Acids and Modification of Parkinsonism. *N. Engl. J. Med.* **276**, 374–379 (1967).
  23. Hornykiewicz, O. Die topische Lokalisation und des Verhalten von Noradrenalin und Dopamin (3-Hydroxytyramin) in der Substantia nigra der normalen und Parkinson Kranken Menschen. *Wien. Klin. Wochschr.* **75**, 309–312 (1963).
  24. Maruthi Prasad, E. & Hung, S. Y. Current therapies in clinical trials of parkinson's disease: A 2021 update. *Pharmaceuticals* **14**, (2021).
  25. Iwai, A. *et al.* The precursor protein of non-A $\beta$  component of Alzheimer's disease amyloid is a presynaptic protein of the central nervous system. *Neuron* **14**, 467–475 (1995).
  26. Jakes, R., Spillantini, M. G. & Goedert, M. Identification of two distinct synucleins from human brain. *FEBS Lett.* **345**, 27–32 (1994).
  27. Ueda, K. *et al.* Molecular cloning of cDNA encoding an unrecognized component of amyloid in Alzheimer disease. *Proc. Natl. Acad. Sci. U. S. A.* **90**, 11282–11286 (1993).
  28. Bussell, R. & Eliezer, D. A structural and functional role for 11-mer repeats in  $\alpha$ -synuclein and other exchangeable lipid binding proteins. *J. Mol. Biol.* **329**, 763–778 (2003).
  29. El-Agnaf, O. M. A. *et al.* Aggregates from mutant and wild-type  $\alpha$ -synuclein proteins and NAC peptide induce apoptotic cell death in human neuroblastoma cells by formation of  $\beta$ -sheet and amyloid-like filaments. *FEBS Lett.* **440**, 71–75 (1998).
  30. Han, H., Weinreb, P. H. & Lansbury, P. T. The core Alzheimer's peptide NAC forms amyloid fibrils which seed and are seeded by  $\beta$ -amyloid: is NAC a common trigger or target in neurodegenerative disease? *Chem. Biol.* **2**, 163–169 (1995).
  31. Lautenschläger, J. *et al.* C-terminal calcium binding of  $\alpha$ -synuclein modulates synaptic vesicle interaction. *Nat. Commun.* **9**, (2018).
  32. Barrett, P. J. & Timothy Greenamyre, J. Post-translational modification of  $\alpha$ -synuclein in Parkinson's disease. *Brain Res.* **1628**, 247–253 (2015).
  33. Burré, J. *et al.*  $\alpha$ -Synuclein promotes SNARE-complex assembly in vivo and

- in vitro. *Science* **329**, 1663–1667 (2010).
34. Nemani, V. M. *et al.* Increased Expression of  $\alpha$ -Synuclein Reduces Neurotransmitter Release by Inhibiting Synaptic Vesicle Reclustering after Endocytosis. *Neuron* **65**, 66–79 (2010).
  35. Swant, J. *et al.*  $\alpha$ -Synuclein Stimulates a Dopamine Transporter-Dependent Chloride Current and Modulates the Activity of the Transporter. *J. Biol. Chem.* **286**, 43933–43943 (2011).
  36. Lou, X., Kim, J., Hawk, B. J. & Shin, Y. K.  $\alpha$ -Synuclein may cross-bridge v-SNARE and acidic phospholipids to facilitate SNARE-dependent vesicle docking. *Biochem. J.* **474**, 2039–2049 (2017).
  37. Perez, R. G. *et al.* A role for  $\alpha$ -synuclein in the regulation of dopamine biosynthesis. *J. Neurosci.* **22**, 3090–3099 (2002).
  38. Scott, D. & Roy, S.  $\alpha$ -Synuclein inhibits intersynaptic vesicle mobility and maintains recycling-pool homeostasis. *J. Neurosci.* **32**, 10129–10135 (2012).
  39. Yu, S. *et al.* Inhibition of tyrosine hydroxylase expression in  $\alpha$ -synuclein-transfected dopaminergic neuronal cells. *Neurosci. Lett.* **367**, 34–39 (2004).
  40. Chandra, S. *et al.* Double-knockout mice for alpha- and beta-synucleins: Effect on synaptic functions. *PNAS* **101**, 14966–71 (2004).
  41. Greten-Harrison, B. *et al.*  $\alpha\beta\gamma$ -Synuclein triple knockout mice reveal age-dependent neuronal dysfunction. *Proc. Natl. Acad. Sci. U. S. A.* **107**, 19573–19578 (2010).
  42. Gedalya, T. Ben *et al.*  $\alpha$ -Synuclein and polyunsaturated fatty acids promote clathrin-mediated endocytosis and synaptic vesicle recycling. *Traffic* **10**, 218–234 (2009).
  43. Liu, S. *et al.*  $\alpha$ -Synuclein Produces a Long-Lasting Increase in Neurotransmitter Release. *EMBO J.* **23**, 4506–4516 (2004).
  44. Vargas, K. J. *et al.* Synucleins regulate the kinetics of synaptic vesicle endocytosis. *J. Neurosci.* **34**, 9364–9376 (2014).
  45. Abeliovich, A. *et al.* Mice Lacking Alpha-Synuclein Display Functional Deficits in the Nigrostriatal Dopamine System. *Neuron* **25**, 239–252 (2000).
  46. Murphy, D. D., Rueter, S. M., Trojanowski, J. Q. & Lee, V. M. Y. Synucleins are developmentally expressed, and  $\alpha$ -synuclein regulates the size of the presynaptic vesicular pool in primary hippocampal neurons. *J. Neurosci.* **20**, 3214–3220 (2000).
  47. Eliezer, D., Kutluay, E., Bussell, R. & Browne, G. Conformational properties of  $\alpha$ -synuclein in its free and lipid-associated states. *J. Mol. Biol.* **307**, 1061–1073 (2001).
  48. Uversky, V. N. A protein-chameleon: Conformational plasticity of  $\alpha$ -synuclein, a disordered protein involved in neurodegenerative disorders. *J. Biomol. Struct. Dyn.* **21**, 211–234 (2003).
  49. Bartels, T., Choi, J. G. & Selkoe, D. J.  $\alpha$ -Synuclein occurs physiologically as a helically folded tetramer that resists aggregation. *Nature* **477**, 107–111 (2011).
  50. Fauvet, B. *et al.*  $\alpha$ -Synuclein in central nervous system and from erythrocytes, mammalian cells, and *Escherichia coli* exists predominantly as disordered monomer. *J. Biol. Chem.* **287**, 15345–15364 (2012).
  51. Serpell, L. C., Berriman, J., Jakes, R., Goedert, M. & Crowther, R. A. Fiber

- diffraction of synthetic  $\alpha$ -synuclein filaments shows amyloid-like cross- $\beta$  conformation. *Proc. Natl. Acad. Sci. U. S. A.* **97**, 4897–4902 (2000).
52. Vilar, M. *et al.* The fold of  $\alpha$ -synuclein fibrils. *Proc. Natl. Acad. Sci. U. S. A.* **105**, 8637–8642 (2008).
  53. Rockenstein, E. *et al.* Accumulation of oligomer-prone  $\alpha$ -synuclein exacerbates synaptic and neuronal degeneration in vivo. *Brain* **137**, 1496–1513 (2014).
  54. Winner, B. *et al.* In vivo demonstration that  $\alpha$ -synuclein oligomers are toxic. *PNAS* **108**, 4194–4199 (2011).
  55. Danzer, K. M. *et al.* Different species of  $\alpha$ -synuclein oligomers induce calcium influx and seeding. *J. Neurosci.* **27**, 9220–9232 (2007).
  56. Hsu, L. J. *et al.*  $\alpha$ -Synuclein Promotes Mitochondrial Deficit and Oxidative Stress. *Am. J. Pathol.* **157**, 401–410 (2000).
  57. Schulz-Schaeffer, W. J. The synaptic pathology of  $\alpha$ -synuclein aggregation in dementia with Lewy bodies, Parkinson's disease and Parkinson's disease dementia. *Acta Neuropathol.* **120**, 131–143 (2010).
  58. Anderson, J. P. *et al.* Phosphorylation of Ser-129 is the dominant pathological modification of  $\alpha$ -synuclein in familial and sporadic lewy body disease. *J. Biol. Chem.* **281**, 29739–29752 (2006).
  59. Smith, W. W. *et al.*  $\alpha$ -synuclein phosphorylation enhances eosinophilic cytoplasmic inclusion formation in SH-SY5Y cells. *J. Neurosci.* **25**, 5544–5552 (2005).
  60. Maurer, K., Volk, S. & Gerbaldo, H. Auguste D and Alzheimer's disease. *Lancet* **349**, 1546–1549 (1997).
  61. Hardy, J. & Allsop, D. Amyloid deposition as the central event in the aetiology of Alzheimer's disease. *Trends Pharmacol. Sci.* **12**, 383–388 (1991).
  62. Braak, H. & Braak, E. Demonstration of Amyloid Deposits and Neurofibrillary Changes in Whole Brain Sections. *Brain Pathol.* **1**, 213–216 (1991).
  63. Wyss-Coray, T. & Rogers, J. Inflammation in Alzheimer disease - A brief review of the basic science and clinical literature. *Cold Spring Harb. Perspect. Med.* **2**, 1–24 (2012).
  64. Kanaan, N. M. *et al.* Axonal degeneration in Alzheimer's disease: When signaling abnormalities meet the axonal transport system. *Exp. Neurol.* **246**, 44–53 (2013).
  65. Ball, M. J. Neuronal Loss, Neurofibrillary Tangles and Granulovacuolar Degeneration in the Hippocampus with Ageing and Dementia. *Acta Neuropathol.* **37**, 111–118 (1977).
  66. DeKosky, S. T. & Scheff, S. W. Synapse loss in frontal cortex biopsies in Alzheimer's disease: Correlation with cognitive severity. *Ann. Neurol.* **27**, 457–464 (1990).
  67. Jr, C. R. J. *et al.* Introduction to revised criteria for the diagnosis of Alzheimer's disease: National Institute on Aging and the Alzheimer Association Workgroups. *Alzheimer Dement.* **7**, 257–262 (2011).
  68. McKhann, G. *et al.* The diagnosis of dementia due to Alzheimer's disease: Recommendations from the National Institute on Aging-Alzheimer's Association workgroups on diagnostic guidelines for Alzheimer's disease *Alzheimers Dement* **7**, 263–269 (2011).

69. Hebert, L. E., Weuve, J., Scherr, P. A. & Evans, D. A. Alzheimer disease in the United States (2010-2050) estimated using the 2010 census. *Neurology* **80**, 1778–1783 (2013).
70. Niu, H., Álvarez-Álvarez, I., Guillén-Grima, F. & Aguinaga-Ontoso, I. Prevalence and incidence of Alzheimer's disease in Europe: A meta-analysis. *Neurol. (English Ed.)* **32**, 523–532 (2017).
71. Mielke, M. M. Sex and Gender Differences in Alzheimer's Disease. *Psychiatr. Times* **35**, 14–17 (2018).
72. Goveas, J. S., Espeland, A. M. A., Woods, N. F., Wassertheil-smoller, S. & Kotchen, J. M. Depressive Symptoms and Incidence of Mild Cognitive Impairment Initiative Memory Study. *J. Am. Geriatr. Soc.* **59**, 57–66 (2011).
73. van Dyck, C. H. *et al.* Lecanemab in Early Alzheimer's Disease. *N. Engl. J. Med.* **388**, 9–21 (2023).
74. Budd Haeberlein, S. *et al.* Two Randomized Phase 3 Studies of Aducanumab in Early Alzheimer's Disease. *J. Prev. Alzheimer's Dis.* **9**, 197–210 (2022).
75. Vassar, R. *et al.*  $\beta$ -Secretase cleavage of Alzheimer's amyloid precursor protein by the transmembrane aspartic protease BACE. *Science* **286**, 735–741 (1999).
76. Bitan, G. *et al.* Amyloid  $\beta$ -protein (A $\beta$ ) assembly: A $\beta$ 40 and A $\beta$ 42 oligomerize through distinct pathways. *Proc. Natl. Acad. Sci. U. S. A.* **100**, 330–335 (2003).
77. Yan, Y. & Wang, C. A $\beta$ 42 is More Rigid than A $\beta$ 40 at the C Terminus: Implications for A $\beta$  Aggregation and Toxicity. *J. Mol. Biol.* **364**, 853–862 (2006).
78. Palmqvist, S. *et al.* Cerebrospinal fluid and plasma biomarker trajectories with increasing amyloid deposition in Alzheimer's disease. *EMBO Mol. Med.* **11**, 1–13 (2019).
79. Serpell, L. C. Alzheimer's amyloid fibrils: Structure and assembly. *Biochimica et Biophysica Acta - Molecular Basis of Disease* **1502**, 16–30 (2000).
80. Hardy, J. & Selkoe, D. J. The amyloid hypothesis of Alzheimer's disease: Progress and problems on the road to therapeutics. *Science* **297**, 353–356 (2002).
81. Huang, X. *et al.* The A $\beta$  peptide of Alzheimer's disease directly produces hydrogen peroxide through metal ion reduction. *Biochemistry* **38**, 7609–7616 (1999).
82. Gunn, A. P. *et al.* Amyloid- $\beta$  Peptide A $\beta$ 3pE-42 Induces Lipid Peroxidation, Membrane Permeabilization, and Calcium Influx in Neurons. *J. Biol. Chem.* **291**, 6134–6145 (2016).
83. Manczak, M. *et al.* Mitochondria are a direct site of A $\beta$  accumulation in Alzheimer's disease neurons: Implications for free radical generation and oxidative damage in disease progression. *Hum. Mol. Genet.* **15**, 1437–1449 (2006).
84. Yasumoto, T. *et al.* High molecular weight amyloid  $\beta$ 1-42 oligomers induce neurotoxicity via plasma membrane damage. *FASEB J.* **33**, 9220–9234 (2019).
85. Walsh, D. M. *et al.* Naturally secreted oligomers of amyloid  $\beta$  protein potently

- inhibit hippocampal long-term potentiation in vivo. *Nature* **416**, 535–539 (2002).
86. Guan, J. S. *et al.* HDAC2 negatively regulates memory formation and synaptic plasticity. *Nature* **459**, 55–60 (2009).
  87. Miśkiewicz, K. *et al.* ELP3 controls active zone morphology by acetylating the ELKS family member bruchpilot. *Neuron* **72**, 776–788 (2011).
  88. Han, Q. *et al.* Gcn5- and Elp3-induced histone H3 acetylation regulates hsp70 gene transcription in yeast. *Biochem. J.* **409**, 779–788 (2008).
  89. Masliah, E., Crews, L. & Hansen, L. Synaptic remodeling during aging and in Alzheimer's disease. *J. Alzheimer's Dis.* **9**, 91–99 (2006).
  90. Scheff, S. W. & Price, D. A. Alzheimer's disease-related synapse loss in the cingulate cortex. *J. Alzheimer's Dis.* **3**, 495–505 (2001).
  91. Geinisman, Y., de Toledo-Morrell, L., Morrell, F., Persina, I. S. & Rossi, M. Age-related loss of axospinous synapses formed by two afferent systems in the rat dentate gyrus as revealed by the unbiased stereological disector technique. *Hippocampus* **2**, 437–444 (1992).
  92. Bloss, E. B. *et al.* Evidence for reduced experience-dependent dendritic spine plasticity in the aging prefrontal cortex. *J. Neurosci.* **31**, 7831–7839 (2011).
  93. Dumitriu, D. *et al.* Selective Changes in Thin Spine Density and Morphology in Monkey Prefrontal Cortex Correlate with Aging-Related Cognitive Impairment. *J. Neurosci.* **30**, 7507–7515 (2010).
  94. Matsuzaki, M., Honkura, N., Ellis-Davies, G. C. R. & Kasai, H. Structural basis of long-term potentiation in single dendritic spines. *Nature* **429**, 761–766 (2004).
  95. Burke, S. N. & Barnes, C. A. Senescent synapses and hippocampal circuit dynamics. *Trends Neurosci.* **33**, 153–161 (2010).
  96. Terry, R. D. *et al.* Physical basis of cognitive alterations in Alzheimer's disease: Synapse loss is the major correlate of cognitive impairment. *Ann. Neurol.* **30**, 572–580 (1991).
  97. Von Bohlen und Halbach, O., Zacher, C., Gass, P. & Unsicker, K. Age-Related Alterations in Hippocampal Spines and Deficiencies in Spatial Memory in Mice. *J. Neurosci. Res.* **83**, 525–531 (2006).
  98. West, M. J., Coleman, P. D., Flood, D. G. & Troncoso, J. C. Differences in the pattern of hippocampal neuronal loss in normal ageing and Alzheimer's disease. *Lancet* **344**, 769–772 (1994).
  99. Penner, M. R., Roth, T. L., Barnes, C. A. & Sweatt, J. D. An epigenetic hypothesis of aging-related cognitive dysfunction. *Front. Aging Neurosci.* **2**, 1–11 (2010).
  100. Morrison, J. H. & Hof, P. R. Selective vulnerability of corticocortical and hippocampal circuits in aging and Alzheimer's disease. *Prog. Brain Res.* **136**, 467–486 (2002).
  101. Klunk, W. E. *et al.* Imaging Brain Amyloid in Alzheimer's Disease with Pittsburgh Compound-B. *Ann. Neurol.* **55**, 306–319 (2004).
  102. Mathis, C. A. *et al.* Synthesis and evaluation of <sup>11</sup>C-labeled 6-substituted 2-arylbenzothiazoles as amyloid imaging agents. *J. Med. Chem.* **46**, 2740–2754 (2003).
  103. Choi, S. R. *et al.* Preclinical Properties of <sup>18</sup>F-AV-45: A PET Agent for A $\beta$

- Plaques in the brain. *J. Nucl. Med.* **50**, 1887-1894 (2009).
104. Lin, K. J. *et al.* Whole-body biodistribution and brain PET imaging with [<sup>18</sup>F]AV-45, a novel amyloid imaging agent - a pilot study. *Nucl. Med. Biol.* **37**, 497–508 (2010).
  105. Rowe, C. C. *et al.* Imaging of amyloid  $\beta$  in Alzheimer's disease with <sup>18</sup>F-BAY94-9172, a novel PET tracer: proof of mechanism. *Lancet Neurol.* **7**, 129–135 (2008).
  106. Koole, M. *et al.* Whole-body biodistribution and radiation dosimetry of <sup>18</sup>F-GE067: A radioligand for in vivo brain amyloid imaging. *J. Nucl. Med.* **50**, 818–822 (2009).
  107. Morris, E. *et al.* Diagnostic accuracy of <sup>18</sup>F amyloid PET tracers for the diagnosis of Alzheimer's disease: a systematic review and meta-analysis. *Eur. J. Nucl. Med. Mol. Imaging* **43**, 374–385 (2016).
  108. Ye, L. *et al.* In vitro high affinity  $\alpha$ -synuclein binding sites for the amyloid imaging agent PIB are not matched by binding to Lewy bodies in postmortem human brain. *J. Neurochem.* **105**, 1428–1437 (2008).
  109. Herholz, K. & Ebmeier, K. Clinical amyloid imaging in Alzheimer's disease. *Lancet Neurol.* **10**, 667–670 (2011).
  110. Jack, C. R. *et al.* Serial PIB and MRI in normal, mild cognitive impairment and Alzheimer's disease: Implications for sequence of pathological events in Alzheimer's disease. *Brain* **132**, 1355–1365 (2009).
  111. Engler, H. *et al.* Two-year follow-up of amyloid deposition in patients with Alzheimer's disease. *Brain* **129**, 2856–2866 (2006).
  112. Schöll, M. *et al.* Low PiB PET retention in presence of pathologic CSF biomarkers in Arctic APP mutation carriers. *Neurology* **79**, 229–236 (2012).
  113. Leuzy, A. *et al.* Tau PET imaging in neurodegenerative tauopathies—still a challenge. *Mol. Psychiatry* **24**, 1112–1134 (2019).
  114. Arriagada, P. V., Growdon, J. H., Hedley-Whyte, E. T. & Hyman, B. T. Neurofibrillary tangles but not senile plaques parallel duration and severity of Alzheimer's disease. *Neurology* **42**, 631 LP – 631 (1992).
  115. Xia, C. F. *et al.* [<sup>18</sup>F]T807, a novel tau positron emission tomography imaging agent for Alzheimer's disease. *Alzheimer's Dement.* **9**, 666–676 (2013).
  116. Ossenkoppele, R. *et al.* Discriminative accuracy of [<sup>18</sup>F]flortaucipir positron emission tomography for Alzheimer disease vs other neurodegenerative disorders. *JAMA - J. Am. Med. Assoc.* **320**, 1151–1162 (2018).
  117. Binette, A. P. *et al.* Amyloid and Tau Pathology Associations With Personality Traits, Neuropsychiatric Symptoms, and Cognitive Lifestyle in the Preclinical Phases of Sporadic and Autosomal Dominant Alzheimer's Disease. *Biol. Psychiatry* **89**, 776–785 (2021).
  118. Leuzy, A. *et al.* A multicenter comparison of [<sup>18</sup>F]flortaucipir, [<sup>18</sup>F]RO948, and [<sup>18</sup>F]MK6240 tau PET tracers to detect a common target ROI for differential diagnosis. *Eur. J. Nucl. Med. Mol. Imaging* **48**, 2295–2305 (2021).
  119. Ossenkoppele, R. *et al.* Accuracy of Tau Positron Emission Tomography as a Prognostic Marker in Preclinical and Prodromal Alzheimer Disease. A Head-to-Head Comparison Against Amyloid Positron Emission Tomography and Magnetic Resonance Imaging. *JAMA Neurol.* **78**, 961–971 (2021).
  120. Chiotis, K., Dodich, A., Boccardi, M., Festari, C. & Drzezga, A. Clinical

- validity of increased cortical binding of tau ligands of the THK family and PBB3 on PET as biomarkers for Alzheimer's disease in the context of a structured 5-phase development framework. *Eur. J. Nucl. Med. Mol. Imaging* **48**, 2086–2096 (2021).
121. Gogola, A. *et al.* Direct Comparison of the Tau PET Tracers <sup>18</sup>F-MK-6240 and <sup>18</sup>F-Flortaucipir in Human Subjects. *J Nucl Med* **63**, 108–116 (2022).
  122. Kaasinen, V. Striatal Dopamine in Parkinson Disease : A Meta-Analysis of Imaging Studies. *Ann. Neurol.* **82**, 873–882 (2017).
  123. Ito, K. *et al.* Striatal and extrastriatal dysfunction in Parkinson's disease with dementia: A 6-[<sup>18</sup>F]fluoro-L-dopa PET study. *Brain* **125**, 1358–1365 (2002).
  124. Sasaki, T. *et al.* Quantification of dopamine transporter in human brain using PET with <sup>18</sup>F-FE-PE2I. *J. Nucl. Med.* **53**, 1065–1073 (2012).
  125. Korat, Š. *et al.* Alpha-Synuclein PET Tracer Development — An Overview about Current Efforts. *Pharmaceutics* **14**, 847 (2021).
  126. Shahnawaz, M. *et al.* Discriminating  $\alpha$ -synuclein strains in Parkinson's disease and multiple system atrophy. *Nature* **578**, 273–277 (2020).
  127. Guilarte, T. R. TSPO in diverse CNS pathologies and psychiatric disease: A critical review and a way forward. *Pharmacol. Ther.* **194**, 44–58 (2019).
  128. Jucaite, A. *et al.* Effect of the myeloperoxidase inhibitor AZD3241 on microglia: A PET study in Parkinson's disease. *Brain* **138**, 2687–2700 (2015).
  129. Janssen, B. *et al.* Identification of the allosteric P2X7 receptor antagonist [<sup>11</sup>C]SMW139 as a PET tracer of microglial activation. *Sci. Rep.* **8**, 1–10 (2018).
  130. Harada, R. *et al.* <sup>18</sup>F-SMBT-1: A selective and reversible PET tracer for monoamine oxidase-b imaging. *J. Nucl. Med.* **62**, 253–258 (2021).
  131. De Wilde, M. C., Overk, C. R., Sijben, J. W. & Masliah, E. Meta-analysis of synaptic pathology in Alzheimer's disease reveals selective molecular vesicular machinery vulnerability. *Alzheimer's Dement.* **12**, 633–644 (2016).
  132. DeKosky, S. T., Scheff, S. W. & Styren, S. D. Structural correlates of cognition in dementia: Quantification and assessment of synapse change. *Neurodegeneration* **5**, 417–421 (1996).
  133. Steidl, J. V., Gomez-Isla, T., Mariash, A., Ashe, K. H. & Boland, L. M. Altered short-term hippocampal synaptic plasticity in mutant  $\alpha$ -synuclein transgenic mice. *Neuroreport* **14**, 219–223 (2003).
  134. Scheff, S. W., Price, D. A., Schmitt, F. A., DeKosky, S. T. & Mufson, E. J. Synaptic alterations in CA1 in mild Alzheimer disease and mild cognitive impairment. *Neurology* **68**, 1501–1508 (2007).
  135. Scheff, S. W., Price, D. A., Schmitt, F. A. & Mufson, E. J. Hippocampal synaptic loss in early Alzheimer's disease and mild cognitive impairment. *Neurobiol. Aging* **27**, 1372–1384 (2006).
  136. Estrada, S. *et al.* [<sup>11</sup>C]UCB-A, a novel PET tracer for synaptic vesicle protein 2A. *Nucl. Med. Biol.* **43**, 325–332 (2016).
  137. Finnema, S. J. *et al.* Imaging synaptic density in the living human brain. *Sci. Transl. Med.* **8**, (2016).
  138. Heurling, K. *et al.* Synaptic vesicle protein 2A as a potential biomarker in synaptopathies. *Mol. Cell. Neurosci.* **97**, 34–42 (2019).
  139. Cai, Z., Li, S., Matuskey, D., Nabulsi, N. & Huang, Y. PET imaging of

- synaptic density: A new tool for investigation of neuropsychiatric diseases. *Neurosci. Lett.* **691**, 44–50 (2019).
140. Constantinescu, C. C. *et al.* Development and In Vivo Preclinical Imaging of Fluorine-18-Labeled Synaptic Vesicle Protein 2A (SV2A) PET Tracers. *Mol. Imaging Biol.* **21**, 509–518 (2019).
  141. Li, S. *et al.* Synthesis and in vivo evaluation of [<sup>18</sup>F]UCB-J for PET imaging of synaptic vesicle glycoprotein 2A (SV2A). *Eur. J. Nucl. Med. Mol. Imaging* **46**, 1952–1965 (2019).
  142. Bajjalieh, S. M., Frantz, G. D., Weimann, J. M., McConnell, S. K. & Scheller, R. H. Differential expression of synaptic vesicle protein 2 (SV2) isoforms. *J. Neurosci.* **14**, 5223–5235 (1994).
  143. Crèvecoeur, J. *et al.* Expression of SV2 isoforms during rodent brain development. *BMC Neurosci.* **14**, (2013).
  144. Chen, M. K. *et al.* Assessing Synaptic Density in Alzheimer Disease with Synaptic Vesicle Glycoprotein 2A Positron Emission Tomographic Imaging. *JAMA Neurol.* **75**, 1215–1224 (2018).
  145. Delva, A., Van Weehaeghe, D., Koole, M., Van Laere, K. & Vandenberghe, W. Loss of Presynaptic Terminal Integrity in the Substantia Nigra in Early Parkinson’s Disease. *Mov. Disord.* **35**, 1977–1986 (2020).
  146. Nicastro, N. *et al.* <sup>11</sup>C-UCB-J synaptic PET and multimodal imaging in dementia with Lewy bodies. *Eur. J. Hybrid Imaging* **4**, (2020).
  147. Thomsen, M. B. *et al.* In vivo imaging of synaptic SV2A protein density in healthy and striatal-lesioned rats with [<sup>11</sup>C]UCB-J PET. *J. Cereb. Blood Flow Metab.* **0**, 1–12 (2020).
  148. Toyonaga, T. *et al.* In vivo synaptic density imaging with <sup>11</sup>C-UCB-J detects treatment effects of saracatinib in a mouse model of Alzheimer disease. *J. Nucl. Med.* **60**, 1780–1786 (2019).
  149. Matuskey, D. *et al.* Synaptic Changes in Parkinson Disease Assessed with in vivo Imaging. *Ann. Neurol.* **87**, 329–338 (2020).
  150. Andersen, K. B. *et al.* Healthy brain aging assessed with [<sup>18</sup>F]FDG and [<sup>11</sup>C]UCB-J PET. *Nucl. Med. Biol.* **112–113**, 52–58 (2022).
  151. Michiels, L. *et al.* Synaptic density in healthy human aging is not influenced by age or sex : a <sup>11</sup>C-UCB-J PET study. *Neuroimage* **232**, 117877 (2021).
  152. Fang, X. T. *et al.* Identifying brain networks in synaptic density PET (<sup>11</sup>C-UCB-J) with independent component analysis. *Neuroimage* **237**, 118167 (2021).
  153. Fiala, M. *et al.* Cyclooxygenase-2-positive macrophages infiltrate the Alzheimer’s disease brain and damage the blood-brain barrier. *Eur. J. Clin. Invest.* **32**, 360–371 (2002).
  154. Librizzi, L., Noè, F., Vezzani, A., De Curtis, M. & Ravizza, T. Seizure-induced brain-borne inflammation sustains seizure recurrence and blood-brain barrier damage. *Ann. Neurol.* **72**, 82–90 (2012).
  155. Zhao, Z., Nelson, A. R., Betsholtz, C. & Zlokovic, B. V. Establishment and Dysfunction of the Blood-Brain Barrier. *Cell* **163**, 1064–1078 (2015).
  156. Persidsky, Y., Ramirez, S. H., Haorah, J. & Kanmogne, G. D. Blood-brain barrier: Structural components and function under physiologic and pathologic conditions. *J. Neuroimmune Pharmacol.* **1**, 223–236 (2006).

157. Armulik, A. *et al.* Pericytes regulate the blood-brain barrier. *Nature* **468**, 557–561 (2010).
158. Tao-Cheng, J. H., Nagy, Z. & Brightman, M. W. Tight junctions of brain endothelium in vitro are enhanced by astroglia. *J. Neurosci.* **7**, 3293–3299 (1987).
159. Lee, E. J., Hung, Y. C. & Lee, M. Y. Early alterations in cerebral hemodynamics, brain metabolism, and blood-brain barrier permeability in experimental intracerebral hemorrhage. *J. Neurosurg.* **91**, 1013–1019 (1999).
160. Tontsch, U. & Bauer, H. C. Glial cells and neurons induce blood-brain barrier related enzymes in cultured cerebral endothelial cells. *Brain Res.* **539**, 247–253 (1991).
161. Georgieva, J. V., Hoekstra, D. & Zuhorn, I. S. Smuggling drugs into the brain: An overview of ligands targeting transcytosis for drug delivery across the blood-brain barrier. *Pharmaceutics* **6**, 557–583 (2014).
162. Van De Bittner, G. C., Ricq, E. L. & Hooker, J. M. A philosophy for CNS radiotracer design. *Acc. Chem. Res.* **47**, 3127–3134 (2014).
163. Murugan, N. A. *et al.* Cross-interaction of tau PET tracers with monoamine oxidase B: evidence from in silico modelling and in vivo imaging. *Eur. J. Nucl. Med. Mol. Imaging* **46**, 1369–1382 (2019).
164. Lockhart, A. *et al.* Evidence for the presence of three distinct binding sites for the thioflavin T class of Alzheimer’s disease PET imaging agents on  $\beta$ -amyloid peptide fibrils. *J. Biol. Chem.* **280**, 7677–7684 (2005).
165. Alafuzoff, I. & Libard, S. Mixed Brain Pathology Is the Most Common Cause of Cognitive Impairment in the Elderly. *J. Alzheimer’s Dis.* **78**, 453–465 (2020).
166. Edison, P. *et al.* Amyloid load in Parkinson’s disease dementia and Lewy body dementia measured with [<sup>11</sup>C]PIB positron emission tomography. *J. Neurol. Neurosurg. Psychiatry* **79**, 1331–1338 (2008).
167. Boerman, O. C. & Oyen, W. J. G. Immuno-PET of cancer: A revival of antibody imaging. *J. Nucl. Med.* **52**, 1171–1172 (2011).
168. Bard F *et al.* Peripherally administered antibodies against amyloid beta-peptide enter the central nervous system and reduce pathology in a mouse model of Alzheimer disease. *Nat. Med.* **6**, 916–919 (2000).
169. Boado, R. J., Zhang, Y., Wang, Y. & Pardridge, W. M. Engineering and Expression of a Chimeric Transferrin Receptor Monoclonal Antibody for Blood-Brain Barrier Delivery in the Mouse. *Biotechnol Bioeng.* **102**, 1251–1258 (2008).
170. Friden, P. M. *et al.* Anti-transferrin receptor antibody and antibody-drug conjugates cross the blood-brain barrier. *Proc. Natl. Acad. Sci. U. S. A.* **88**, 4771–4775 (1991).
171. Pardridge, W. M., Kang, Y.-S., Buciak, J. L. & Yang, J. Human insulin receptor monoclonal antibody undergoes high affinity binding to human brain capillaries in vitro.pdf. *Pharmacological research* **12**, 807–816 (1995).
172. Shen, Y. *et al.* Delivery of liposomes with different sizes to mice brain after sonication by focused ultrasound in the presence of microbubbles. *Ultrasound Med. Biol.* **42**, 1499–1511 (2016).
173. Boado, R. J., Zhou, Q. H., Lu, J. Z., Hui, E. K. W. & Pardridge, W. M.

- Pharmacokinetics and brain uptake of a genetically engineered bifunctional fusion antibody targeting the mouse transferrin receptor. *Mol. Pharm.* **7**, 237–244 (2010).
174. Pardridge, W. M. Molecular Trojan horses for blood-brain barrier drug delivery. *Curr. Opin. Pharmacol.* **6**, 494–500 (2006).
  175. Yu, Y. J. *et al.* Therapeutic bispecific antibodies cross the blood-brain barrier in nonhuman primates. *Sci. Transl. Med.* **6**, 1–11 (2014).
  176. Stergiou, N. *et al.* Application of <sup>89</sup>Zr-DFO\*-immuno-PET to assess improved target engagement of a bispecific anti-amyloid- $\beta$  monoclonal antibody. *Eur. J. Nucl. Med. Mol. Imaging* online (2023). doi: 10.1007/s00259-023-06109-3
  177. Fang, X. T. *et al.* High detection sensitivity with antibody-based PET radioligand for amyloid beta in brain. *Neuroimage* **184**, 881–888 (2019).
  178. Sehlin, D. *et al.* Antibody-based PET imaging of amyloid beta in mouse models of Alzheimer’s disease. *Nat. Commun.* **7**, 1–11 (2016).
  179. Hultqvist, G., Syvänen, S., Fang, X. T., Lannfelt, L. & Sehlin, D. Bivalent brain shuttle increases antibody uptake by monovalent binding to the transferrin receptor. *Theranostics* **7**, 308–318 (2017).
  180. Kissel, K. *et al.* Immunohistochemical localization of the murine transferrin receptor (TfR) on blood-tissue barriers using a novel anti-TfR monoclonal antibody. *Histochem. Cell Biol.* **110**, 63–72 (1998).
  181. Lee, H. J., Engelhardt, B., Lesley, J., Bickel, U. & Pardridge, W. M. Targeting rat anti-mouse transferrin receptor monoclonal antibodies through blood-brain barrier in mouse. *J. Pharmacol. Exp. Ther.* **292**, 1048–1052 (2000).
  182. Okuyama, T. *et al.* A Phase 2/3 Trial of Pabinafusp Alfa, IDS Fused with Anti-Human Transferrin Receptor Antibody, Targeting Neurodegeneration in MPS-II. *Mol. Ther.* **29**, 671–679 (2021).
  183. Sehlin, D. & Syvänen, S. Engineered antibodies: new possibilities for brain PET? *Eur. J. Nucl. Med. Mol. Imaging* **11**, (2019).
  184. van Lengerich, B. *et al.* A TREM2-activating antibody with a blood-brain barrier transport vehicle enhances microglial metabolism in Alzheimer’s disease models. *Nat. Neurosci.* online (2023). doi:10.1038/s41593-022-01240-0
  185. Bateman, A. *et al.* UniProt: the universal protein knowledgebase in 2021. *Nucleic Acids Res.* **49**, D480–D489 (2021).
  186. Faresjö, R., Bonvicini, G., Fang, X. T., Aguilar, X. & Sehlin, D. Brain pharmacokinetics of two BBB penetrating bispecific antibodies of different size. *Fluids Barriers CNS* **18**, (2021).
  187. Cook, B. E. *et al.* Non-invasive Imaging of Antisense Oligonucleotides in the Brain via In Vivo Click Chemistry. *Mol. Imaging Biol.* **24**, 940–949 (2022).
  188. Altai, M., Membreno, R., Cook, B., Tolmachev, V. & Zeglis, B. M. Pretargeted imaging and therapy. *J. Nucl. Med.* **58**, 1553–1559 (2017).
  189. Lashuel, H. A., Overk, C. R., Oueslati, A. & Masliah, E. The many faces of  $\alpha$ -synuclein: From structure and toxicity to therapeutic target. *Nat. Rev. Neurosci.* **14**, 38–48 (2013).
  190. Gunn, R. N., Gunn, S. R. & Cunningham, V. J. Positron emission tomography compartmental models. *J. Cereb. Blood Flow Metab.* **21**, 635–652 (2001).

191. Innis, R. B. *et al.* Consensus nomenclature for in vivo imaging of reversibly binding radioligands. *J. Cereb. Blood Flow Metab.* **27**, 1533–1539 (2007).
192. Lammertsma, A. A. & Hume, S. P. Simplified reference tissue model for PET receptor studies. *Neuroimage* **4**, 153–158 (1996).
193. Lanz, B., Poitry-Yamate, C. & Gruetter, R. Image-derived input function from the vena cava for <sup>18</sup>F-FDG PET studies in rats and mice. *J. Nucl. Med.* **55**, 1380–1388 (2014).
194. Alf, M. F. *et al.* Quantification of brain glucose metabolism by <sup>18</sup>F-FDG PET with real-time arterial and image-derived input function in mice. *J. Nucl. Med.* **54**, 132–138 (2013).
195. Verhaeghe, J. *et al.* Noninvasive Relative Quantification of [<sup>11</sup>C]ABP688 PET Imaging in Mice Versus an Input Function Measured Over an Arteriovenous Shunt. *Front. Neurol.* **9**, 516 (2018).
196. Bertoglio, D. *et al.* Validation and noninvasive kinetic modeling of [<sup>11</sup>C]UCB-J PET imaging in mice. *J. Cereb. Blood Flow Metab.* **0**, 1–12 (2019).
197. Zanotti-Fregonara, P., Chen, K., Liow, J.-S., Fujita, M. & Innis, R. B. Image-derived input function for brain PET studies: many challenges and few opportunities. *J. Cereb. Blood Flow Metab.* **31**, 1986–1998 (2011).
198. Bailey, D. L. & Townsend, D. W. *Positron Emission Tomography: basic sciences.* (Springer Science & Business Media, 2004).
199. Kahle, P. J. *et al.* Subcellular Localization of Wild-Type and Parkinson’s Disease-Associated Mutant  $\alpha$ -Synuclein in Human and Transgenic Mouse Brain. *J. Neurosci.* **20**, 6365–6373 (2000).
200. Rockenstein, E. *et al.* Differential neuropathological alterations in transgenic mice expressing  $\alpha$ -synuclein from the platelet-derived growth factor and Thy-1 promoters. *J. Neurosci. Res.* **68**, 568–578 (2002).
201. Lord, A. *et al.* The Arctic Alzheimer mutation facilitates early intraneuronal A $\beta$  aggregation and senile plaque formation in transgenic mice. *Neurobiol. Aging* **27**, 67–77 (2006).
202. Saito, T. *et al.* Single App knock-in mouse models of Alzheimer’s disease. *Nat. Neurosci.* **17**, 661–663 (2014).
203. Chesselet, M. F. *et al.* A Progressive Mouse Model of Parkinson’s Disease: The Thy1- $\alpha$ Syn (‘Line 61’) Mice. *Neurotherapeutics* **9**, 297–314 (2012).
204. Lam, H. A. *et al.* Elevated Tonic Extracellular Dopamine Concentration and Altered Dopamine Modulation of Synaptic Activity Precede Dopamine Loss in the Striatum of Mice Overexpressing Human  $\alpha$ -Synuclein. *Jouranal Neurosci. Res.* **89**, 1090–102 (2011).
205. Roshanbin, S. *et al.* Age-related increase of alpha-synuclein oligomers is associated with motor disturbances in L61 transgenic mice. *Neurobiol. Aging* **101**, 207–220 (2021).
206. Rabl, R. *et al.* Early start of progressive motor deficits in Line 61  $\alpha$ -synuclein transgenic mice. *BMC Neurosci.* **18**, 1–12 (2017).
207. Wrasidlo, W. *et al.* A de novo compound targeting  $\alpha$ -synuclein improves deficits in models of Parkinson’s disease. *Brain* **139**, 3217–3236 (2016).
208. Fleming, S. M. *et al.* Early and progressive sensorimotor anomalies in mice overexpressing wild-type human  $\alpha$ -synuclein. *J. Neurosci.* **24**, 9434–9440 (2004).

209. Price, D. L. *et al.* The small molecule alpha-synuclein misfolding inhibitor, NPT200-11, produces multiple benefits in an animal model of Parkinson's disease. *Sci. Rep.* **8**, 1–12 (2018).
210. Ekmark-Lewén, S. *et al.* Early fine motor impairment and behavioral dysfunction in (Thy-1)-h[A30P] alpha-synuclein mice. *Brain Behav.* **8**, 1–14 (2018).
211. Fagerqvist, T. *et al.* Monoclonal antibodies selective for  $\alpha$ -synuclein oligomers/ protofibrils recognize brain pathology in Lewy body disorders and  $\alpha$ -synuclein transgenic mice with the disease-causing A30P mutation. *J. Neurochem.* **126**, 131–144 (2013).
212. Paiva, I. *et al.* Alpha-synuclein deregulates the expression of COL4A2 and impairs ER-Golgi function. *Neurobiol. Dis.* **119**, 121–135 (2018).
213. Philipson, O. *et al.* Animal models of amyloid- $\beta$ -related pathologies in Alzheimer's disease. *FEBS J.* **277**, 1389–1409 (2010).
214. Lillehaug, S. *et al.* Brainwide distribution and variance of amyloid-beta deposits in tg-ArcSwe mice. *Neurobiol. Aging* **35**, 556–564 (2014).
215. Yu, Y. J. *et al.* Boosting Brain Uptake of a Therapeutic Antibody by Reducing Its Affinity for a Transcytosis Target. *Sci. Transl. Med.* **3**, 1–9 (2011).
216. Fang, X. T., Sehlin, D., Lannfelt, L., Syvänen, S. & Hultqvist, G. Efficient and inexpensive transient expression of multispecific multivalent antibodies in Expi293 cells. *Biol. Proced. Online* **19**, 1–9 (2017).
217. Näsström, T. *et al.* Antibodies against alpha-synuclein reduce oligomerization in living cells. *PLoS One* **6**, 1–8 (2011).
218. Vaikath, N. N. *et al.* Generation and characterization of novel conformation-specific monoclonal antibodies for  $\alpha$ -synuclein pathology. *Neurobiol. Dis.* **79**, 81–99 (2015).
219. Englund, H. *et al.* Sensitive ELISA detection of amyloid- $\beta$  protofibrils in biological samples. *J. Neurochem.* **103**, 334–345 (2007).
220. Lancelot, S. & Zimmer, L. Small-animal positron emission tomography as a tool for neuropharmacology. *Trends Pharmacol. Sci.* **31**, 411–417 (2010).
221. Chu, S. Y. F., Ekström, L. P. & Firestone, R. B. The Lund/LBNL Nuclear Data Search. Table of Radioactive Isotopes (1998). Available at: <http://nucleardata.nuclear.lu.se/toi/>.
222. Moses, W. W. Fundamental limits of spatial resolution in PET. *Nucl. Instruments Methods Phys. Res. Sect. A Accel. Spectrometers, Detect. Assoc. Equip.* **648**, S236–S240 (2011).
223. Pentlow, K. S. *et al.* Quantitative Imaging of Iodine-124 with PET. *J Nucl Med* **37**, 1557–1562 (1996).
224. Rokka, J., Schlein, E. & Eriksson, J. Improved synthesis of SV2A targeting radiotracer [ $^{11}\text{C}$ ]UCB-J. *EJNMMI Radiopharm. Chem.* **4**, (2019).
225. Li, S. *et al.* Synthesis and in Vivo Evaluation of a Novel PET Radiotracer for Imaging of Synaptic Vesicle Glycoprotein 2A (SV2A) in Nonhuman Primates. *ACS Chem. Neurosci.* **10**, 1544–1554 (2019).
226. Zheng, C. *et al.* A metabolically stable PET tracer for imaging synaptic vesicle protein 2A: synthesis and preclinical characterization of [ $^{18}\text{F}$ ]SDM-16. *Eur. J. Nucl. Med. Mol. Imaging* **49**, 1482–1496 (2022).
227. Greenwood, F. C., Hunter, W. M. & Glover, J. S. The Preparation of  $^{131}\text{I}$ -

- Labelled Human Growth Hormone of High Specific Radioactivity. *Biochem. J.* **89**, 114–123 (1963).
228. Fahey, F. H. Data acquisition in PET imaging. *J. Nucl. Med. Technol.* **30**, 39–49 (2002).
229. Conti, M. State of the art and challenges of time-of-flight PET. *Phys. Medica* **25**, 1–11 (2009).
230. Suetens, P. *Fundamentals of medical imaging. Fundamentals of Medical Imaging* (Cambridge university press, 2017). doi:10.1017/9781316671849
231. Ma, Y. *et al.* A three-dimensional digital atlas database of the adult C57BL/6J mouse brain by magnetic resonance microscopy. *Neuroscience* **135**, 1203–1215 (2005).
232. Logan, J. A review of graphical methods for tracer studies and strategies to reduce bias. *Nucl. Med. Biol.* **30**, 833–844 (2003).
233. Logan, J. Graphical analysis of PET data applied to reversible and irreversible tracers. *Nucl. Med. Biol.* **27**, 661–670 (2000).
234. Logan, J. *et al.* Graphical Analysis of Reversible Radioligand Binding from Time-Activity Measurements Applied to [N-<sup>11</sup>C-methyl]-(-)-Cocaine PET Studies in Human Subjects. *J. Cereb. Blood Flow Metab.* **10**, 740–747 (1990).
235. Chang, H. Y. *et al.* Brain pharmacokinetics of anti-transferrin receptor antibody affinity variants in rats determined using microdialysis. *MAbs* **13**, (2021).
236. Roshanbin, S. *et al.* Reduction of  $\alpha$ SYN Pathology in a Mouse Model of PD Using a Brain-Penetrating Bispecific Antibody. *Pharmaceutics* **14**, 1412 (2022).
237. Schiffer, W. K. *et al.* Serial microPET measures of the metabolic reaction to a microdialysis probe implant. *J. Neurosci. Methods* **155**, 272–284 (2006).
238. Chaurasia, C. S. *et al.* AAPS-FDA workshop white paper: Microdialysis principles, application and regulatory perspectives. *Pharm. Res.* **24**, 1014–1025 (2007).
239. Gustafsson, S. *et al.* Blood-brain barrier integrity in a mouse model of Alzheimer’s disease with or without acute 3D6 immunotherapy. *Neuropharmacology* **143**, 1–9 (2018).
240. Josephy, P. D., Eling, T. & Mason, R. P. The horseradish peroxidase-catalyzed oxidation of 3,5,3',5'-tetramethylbenzidine. Free radical and charge-transfer complex intermediates. *J. Biol. Chem.* **257**, 3669–3675 (1982).
241. Xue, C., Lin, T. Y., Chang, D. & Guo, Z. Thioflavin T as an amyloid dye: Fibril quantification, optimal concentration and effect on aggregation. *R. Soc. Open Sci.* **4**, (2017).
242. Huttenlocher, P. R. Synaptic density in human frontal cortex - developmental changes and effects of aging. *Brain Res.* **163**, 195–205 (1979).
243. Taylor, E. N. *et al.* The brains of aged mice are characterized by altered tissue diffusion properties and cerebral microbleeds. *J. Transl. Med.* **18**, 1–11 (2020).
244. Lee, H., GoodSmith, D. & Knierim, J. J. Parallel processing streams in the hippocampus. *Curr. Opin. Neurobiol.* **64**, 127–134 (2020).
245. Burwell, R. D. The parahippocampal region: Corticocortical connectivity. *Ann. N. Y. Acad. Sci.* **911**, 25–42 (2000).

246. Di Maio, V. The glutamatergic synapse: a complex machinery for information processing. *Cogn. Neurodyn.* **15**, 757–781 (2021).
247. Megías, M., Emri, Z., Freund, T. F. & Gulyás, A. I. Total number and distribution of inhibitory and excitatory synapses on hippocampal CA1 pyramidal cells. *Neuroscience* **102**, 527–540 (2001).
248. Vanoye-Carlo, A. & Gómez-Lira, G. Differential expression of SV2A in hippocampal glutamatergic and GABAergic terminals during postnatal development. *Brain Res.* **1715**, 73–83 (2019).
249. Morrison, J. H. & Baxter, M. G. The ageing cortical synapse: Hallmarks and implications for cognitive decline. *Nat. Rev. Neurosci.* **13**, 240–250 (2012).
250. Akkermans, J., Zajicek, F., Miranda, A. & Adhikari, M. Identification of pre-synaptic density networks using SV2A PET imaging and ICA in healthy and diseased mice. *Neuroimage* **264**, 119771 (2022).
251. Sadasivam, P. *et al.* Quantification of SV2A Binding in Rodent Brain Using [<sup>18</sup>F]SynVesT-1 and PET Imaging. *Mol Imaging Biol.* **23**, 372–381 (2021).
252. Mansur, A. *et al.* Characterization of 3 PET tracers for quantification of mitochondrial and synaptic function in healthy human brain: <sup>18</sup>F-BCPP-EF, <sup>11</sup>C-SA-4503, and <sup>11</sup>C-UCB-J. *J. Nucl. Med.* **61**, 96–103 (2020).
253. Bertoglio, D. *et al.* Validation, kinetic modeling, and test-retest reproducibility of [<sup>18</sup>F]SynVesT-1 for PET imaging of synaptic vesicle glycoprotein 2A in mice. *J. Cereb. Blood Flow Metab.* **42**, 1867–1878 (2022).
254. Meier, S. R. *et al.* Antibody-based in vivo PET imaging detects amyloid-β reduction in Alzheimer transgenic mice after BACE-1 inhibition. *J. Nucl. Med.* **59**, 1885–1891 (2018).
255. Meier, S. R. *et al.* <sup>11</sup>C-PIB and <sup>124</sup>I-antibody PET provide differing estimates of brain amyloid-beta after therapeutic intervention. *J. Nucl. Med.* **63**, 302–309 (2021).
256. Moos, T. Immunohistochemical localization of intraneuronal transferrin receptor immunoreactivity in the adult mouse central nervous system. *J. Comp. Neurol.* **375**, 675–692 (1996).
257. Kariolis, M. S. *et al.* Brain delivery of therapeutic proteins using an Fc fragment blood-brain barrier transport vehicle in mice and monkeys. *Sci. Transl. Med.* **12**, 1–14 (2020).
258. Chang, H. Y., Morrow, K., Bonacquisti, E., Zhang, W. Y. & Shah, D. K. Antibody pharmacokinetics in rat brain determined using microdialysis. *MAbs* **10**, 843–853 (2018).
259. Le Priault, F., Barini, E., Laplanche, L., Schlegel, K. & Mezler, M. Collecting antibodies and large molecule biomarkers in mouse interstitial brain fluid: a comparison of microdialysis and cerebral open flow microperfusion. *MAbs* **13**, 1918819 (2021).
260. Swanson, C. J. *et al.* A randomized, double-blind, phase 2b proof-of-concept clinical trial in early Alzheimer’s disease with lecanemab, an anti-Aβ protofibril antibody. *Alzheimer’s Res. Ther.* **13**, 1–14 (2021).
261. Tolar, M., Abushakra, S., Hey, J. A., Porsteinsson, A. & Sabbagh, M. Aducanumab, gantenerumab, BAN2401, and ALZ-801 - The first wave of amyloid-targeting drugs for Alzheimer’s disease with potential for near term approval. *Alzheimer’s Res. Ther.* **12**, 1–10 (2020).

262. WHO. Global Dementia Observatory (GDO). (2016). Available at: <https://apps.who.int/gho/data/node.dementia>.

# Acta Universitatis Upsaliensis

*Digital Comprehensive Summaries of Uppsala Dissertations  
from the Faculty of Medicine 1907*

Editor: The Dean of the Faculty of Medicine

A doctoral dissertation from the Faculty of Medicine, Uppsala University, is usually a summary of a number of papers. A few copies of the complete dissertation are kept at major Swedish research libraries, while the summary alone is distributed internationally through the series Digital Comprehensive Summaries of Uppsala Dissertations from the Faculty of Medicine. (Prior to January, 2005, the series was published under the title “Comprehensive Summaries of Uppsala Dissertations from the Faculty of Medicine”.)

Distribution: [publications.uu.se](http://publications.uu.se)  
urn:nbn:se:uu:diva-497274



ACTA  
UNIVERSITATIS  
UPSALIENSIS  
UPPSALA  
2023